bioRxiv preprint doi: https://doi.org/10.1101/2024.02.16.580716; this version posted February 21, 2024. The copyright holder for this preprint (which was not certified by peer review) is the author/funder, who has granted bioRxiv a license to display the preprint in perpetuity. It is made available under a CC-BY-NC-ND 4.0 International license.

Interplay between Mg^{2+} and Ca^{2+} at multiple sites of the ryanodine receptor

Ashok R. Nayak[1], Warin Rangubpit[2], Alex H. Will[1], Yifan Hu[1], Pablo Castro-Hartmann[1‡], Joshua J. Lobo[1], Kelly Dryden[3], Graham D. Lamb[4], Pornthep Sompornpisut[2], Montserrat Samsó[1*]

Affiliations

[1]Department of Physiology and Biophysics, Virginia Commonwealth University, Richmond, VA, USA.
[2]Department of Chemistry, Faculty of Science, Chulalongkorn University, Bangkok, Thailand.
[3]Department of Molecular Physiology and Biological Physics, University of Virginia, Charlottesville, Virginia, USA.
[4]Department of Microbiology, Anatomy, Physiology and Pharmacology, La Trobe University, Melbourne, Victoria, Australia.
[‡]Present address: ThermoFisher Scientific, Cambridge, United Kingdom.
[*]Correspondence to: montserrat.samso@vcuhealth.org, pornthep.s@chula.ac.th

Abstract

RyR1 is an intracellular Ca^{2+} channel important in excitable cells. Ca^{2+} activates it at low concentrations and inhibits it at high concentrations. Mg^{2+} is the main physiological RyR1 inhibitor, an effect that is overridden upon activation. Despite the significance of Mg^{2+}-mediated inhibition, the molecular-level mechanisms remain unclear. We determined two cryo-EM structures of RyR1 with Mg^{2+} up to 2.8 Å resolution, identifying multiple Mg^{2+} binding sites. Mg^{2+} inhibits at the known Ca^{2+} activating site and we propose that the EF hand domain is an inhibitory divalent cation sensor. Both divalent cations bind to ATP within a crevice, contributing to the precise transmission of allosteric changes within the enormous channel protein. Notably, Mg^{2+} inhibits RyR1 by interacting with the gating helices as validated by molecular dynamics. This structural insight enhances our understanding of how Mg^{2+} inhibition is overcome during excitation.

This manuscript is dedicated to the late Dr. Gerhard Meissner, who pioneered understanding of the role of Mg^{2+} on RyR1 and suggested exploring it at the structural level.

Introduction

Ryanodine receptors (RyRs), the largest ion channels known (2.2 MDa), mediate intracellular Ca^{2+} release from the sarco/endoplasmic reticulum (SR/ER) in excitable and non-excitable cells. Skeletal muscle, which supports voluntary contraction, expresses RyR1, whereas cardiac muscle expresses RyR2. These two RyR isoforms, together with RyR3, are also expressed in brain and other organs (*1-3*). In skeletal muscle, action potentials activate the L-type Ca^{2+} channel ($Ca_V1.1$, also known as dihydropyridine receptor (DHPR)) resulting in RyR1 opening and subsequent muscle contraction, in the process known as excitation-contraction (EC) coupling. The L-type

bioRxiv preprint doi: https://doi.org/10.1101/2024.02.16.580716; this version posted February 21, 2024. The copyright holder for this preprint (which was not certified by peer review) is the author/funder, who has granted bioRxiv a license to display the preprint in perpetuity. It is made available under a CC-BY-NC-ND 4.0 International license.

voltage-gated Ca^{2+} channel works as a sensor located in the T-tubule membrane and activates the RyR1 via conformational coupling (*4, 5*). The RyR pore lacks Ca^{2+} selectivity, allowing co-permeation of other cations such as K^+, Na^+, and Mg^{2+} through the open channel (*6*). Paradoxically, Mg^{2+}, the predominant divalent cation in the cytosol, is a constitutive RyR1 inhibitor. Hence, in the absence of membrane depolarization, muscles are actively kept quiescent by Mg^{2+} (*7-10*). Mg^{2+} inhibits RyRs by unknown mechanism(s), but when the channel is activated, Mg^{2+} permeates through the RyR1 pore and competes with the Ca^{2+} current (*6, 11*). Intracellular Mg^{2+} (about 8 mM in total in the cytoplasm) is mainly complexed in the form of ATP-Mg^{2+} (~7 mM), the physiologically active form of ATP, while 0.9-1.5 mM exists as free Mg^{2+} (*12-14*). Abnormally low free Mg^{2+} cytosolic concentrations result in spontaneous RyR1-mediated Ca^{2+} release (*8, 9*), and impaired regulation of RyR1 by Mg^{2+} confers susceptibility to malignant hyperthermia (MH) (*15, 16*).

Ca^{2+} has a biphasic effect on RyRs (*7*), which is mediated by a high-affinity, activating Ca^{2+}-binding site (*17, 18*) and putative low-affinity Ca^{2+} binding site(s) (*19, 20*). Thus, an intricate control of RyR gating by its ligands in the physiological scenario emerges, where the concentrations of Mg^{2+} and ATP are kept constant but DHPR conformational change and subsequent increase of cytosolic Ca^{2+} concentration constitute the principal activation variables. How the two divalent cations, Mg^{2+} and Ca^{2+}, have such disparate effects on RyR has remained a mystery with several, non-exclusive mechanisms proposed; these include: (a) Mg^{2+} competition at the high-affinity Ca^{2+} activation site producing an opposite effect (*7, 8, 21, 22*), (b) Mg^{2+} and Ca^{2+} binding to low-affinity cytosolic inhibitory sites producing a similar effect (*7, 16, 20*), and (c) competition for ion flow (*6, 21, 23*).

We tested these hypotheses by determining the cryo-EM structures of RyR1 under two concentrations of free Mg^{2+}. [^{3}H] ryanodine (Ry) binding was carried out to examine the response of our purified channels to different combinations of Ca^{2+}, Mg^{2+}, ATP, and ACP, and help to interpret the structural results. RyR1 was reconstituted in lipidic nanodiscs to replicate its membrane-embedded state and eliminate detergent-induced artifacts (*24-26*). A putative Mg^{2+} binding site along the ion pathway was evaluated using molecular dynamics (MD), which illustrated distinct modes of interaction of Ca^{2+} and Mg^{2+} at such site. Our MD-interpreted structures help to clarify the dual effects of Mg^{2+}'s interaction with RyR1, namely permeation and inhibition. In addition, we identified three other binding sites for Mg^{2+} that are shared with Ca^{2+}, where binding of either cation to each site results in distinct effects. Altogether, this work provides fundamental insight into the complex regulation of RyR1 by divalent cations.

Results

Mg^{2+} overrides the activating effects of Ca^{2+} and ATP

We studied the effect of ATP and Mg^{2+} on the Ca^{2+}-induced activity profile of rabbit RyR1 using the tritiated ryanodine ([^{3}H]Ry) binding assay, which reflects the probability of channel opening (*27*). The assay, carried out under a wide range of Ca^{2+} concentrations, indicated typical biphasic response of RyR1 to free Ca^{2+} and a three-fold upregulation by 2 mM ATP at peak RyR1 activation (Fig. 1A). Presence of 1 mM free Mg^{2+} inhibited the channel at all Ca^{2+} concentrations despite the presence of ATP or activating Ca^{2+} conditions (Fig. 1A). In a competition experiment, Mg^{2+}

bioRxiv preprint doi: https://doi.org/10.1101/2024.02.16.580716; this version posted February 21, 2024. The copyright holder for this preprint (which was not certified by peer review) is the author/funder, who has granted bioRxiv a license to display the preprint in perpetuity. It is made available under a CC-BY-NC-ND 4.0 International license.

showed progressive inhibition starting at concentrations well below the physiological concentration of Mg^{2+}, with 50% lower ryanodine binding at a Mg^{2+}/Ca^{2+} ratio of 2.2 (without ATP) and 3.5 (in the presence of 5 mM ATP) (Fig. 1B). The IC_{50} was 111 μM for Mg^{2+} and 174 μM for ATP/Mg^{2+}; EC_{50} for ATP was 848 μM. In agreement with previous studies (*26*), ACP had a stronger activating effect on RyR1 than ATP and, under maximally activating Ca^{2+}, enabled RyR1 activity under conditions of Mg^{2+} that normally fully inhibit the channel in the presence of ATP (Fig. 1C).

Cryo-EM structure determination

Cryo-EM and single-particle analysis was carried out on RyR1 reconstituted in POPC-MSP1E3D1 nanodiscs at two different concentrations of free Mg^{2+}, ~1 mM and ~10 mM, and in the presence of AMP-PNP (ACP), a non-hydrolyzable ATP analog. We refer to such conditions as ACP/LMg^{2+} and ACP/HMg^{2+} henceforth. The overall resolutions for the RyR1-ACP/LMg^{2+} and RyR1-ACP/HMg^{2+} datasets were 4.4 Å and 3.1 Å, respectively, and increased locally using focused refinement. The symmetry-expanded focused map of RyR1-ACP/LMg^{2+} had a resolution of 3.8 Å in the channel's stem region formed by the central domain (CD), U-motif, transmembrane domain (TMD), and C-terminal domain (CTD) (residues 3668-5037). In RyR1-ACP/HMg^{2+}, targeted refinement of the TMD and cytoplasmic assembly (CytA) yielded resolutions of 2.8 and 3.4 Å, respectively. Details on cryo-EM data collection, single-particle image processing, and model quality characteristics are summarized in Figs. S1, S2 and Table S1. Except for the divalent cation and ACP concentration, the buffer conditions are identical to these we used in previous 3D reconstructions relevant for this study, determined either in the absence of divalent (i.e., in a mixture of EGTA and EDTA; henceforth RyR1-ACP/EGTA) or in the presence of 2 mM Ca^{2+} (which yielded an open and an inactivated conformation, henceforth referred to as RyR1-ACP/Ca^{2+}-open and RyR1-ACP/Ca^{2+}-inactivated, respectively) (*26*).

A defining characteristic of RyR1's conformation is the flexion angle (*28*). This angle largely recapitulates the swiveling of the four quadrants of the top shell of the cytoplasmic assembly formed by the NTD, handle, SPRY, HD1, and P1 domains, which reflects structural transitions of the RyR1 upon its modulation by ligands (*29*) and becomes a determining factor in classification of RyR cryo-EM images. The RyR1-ACP/LMg^{2+} 3D structure had a flexion angle of -1.5° (Fig. S1), and further targeted 3D classification utilizing a quadrant-shaped mask in conjunction with symmetry expansion resulted in three main conformations of the cytoplasmic shell, with flexion angles of -0.4° (32%), -1.6° (24%), and -2.0° (33%). The RyR1-ACP/HMg^{2+} dataset had conformation homogeneity and exhibited a larger degree of swiveling with a flexion angle of -2.5°.

Mg^{2+} accommodates at the fourfold axis and constricts the ion permeation pathway

The transmembrane domain of RyR1 has the typical 6-TM organization shared among several cation channels (*29*), where the sixth α-helix (S6, or inner helix) of each of the four subunits assembles as a helical bundle to form the ion permeation pathway. The long C-terminal portion of S6 (S6C') extends the helical bundle into the cytoplasm. Pore profiles of RyR1 under ACP/LMg^{2+} and ACP/HMg^{2+} conditions revealed a closed pore with a radius narrowing to 1 Å at the hydrophobic gate I4937 (Fig. 2). The S6 helix separation at I4937 (measured as distance between

bioRxiv preprint doi: https://doi.org/10.1101/2024.02.16.580716; this version posted February 21, 2024. The copyright holder for this preprint (which was not certified by peer review) is the author/funder, who has granted bioRxiv a license to display the preprint in perpetuity. It is made available under a CC-BY-NC-ND 4.0 International license.

opposite C_α) was 10.6 Å for RyR1-ACP/LMg^{2+} and 10.5 Å for RyR1-ACP/HMg^{2+}, within the narrow range of 10.3-10.6 Å found for other closed structures (RyR1-ACP/EGTA and RyR1-FKBP12/EGTA (*17, 26*)).

The ion permeation pathway revealed non-protein cryo-EM densities along the pore axis, a feature observed in other reconstructions of RyR. Notably, under the high Mg^{2+} condition, a density between the four side chains of D4945 of S6C' became well defined, with the same or higher σ level than the protein density, and much higher than any central density in RyR1-ACP/EGTA (PDB ID: 7K0T) prepared under matching conditions except for the lack of Mg^{2+}. As a comparison, an axial non-protein density in the selectivity filter region had a σ value of 1.75 that did not increase with the Mg^{2+} concentration. The density at position D4945 was substantially higher when compared to other reconstructions such as RyR1-ACP/Ca^{2+} (PDB ID: 5T15), or RyR1-ACP/HCa^{2+} (PDB ID: 7TDG), while RyR1-ACP/LMg^{2+} showed intermediate density, altogether suggesting that the identity of this central density corresponds to Mg^{2+}. Further supporting this assignment, in the absence of Mg^{2+} the side chain carbonyls of D4945 orient away from the fourfold axis, suggesting repulsion among them, whereas in the presence of Mg^{2+} the side chains of D4945 are oriented towards the central globular density (Fig. 3A).

In the absence of Mg^{2+} or Ca^{2+}, there is a hydrogen bond between adjacent S6 helices, R4944-E4942. In RyR1-ACP/LMg^{2+}, the S6 helical bundle tightens, a trend that is enhanced in RyR1-ACP/HMg^{2+}, where the pore further constricts forming a tripartite D4945-R4944-D4938 salt bridge that also connects to the putative Mg^{2+} mass at the level of D4945 (Fig. 3B, Movie S1), also forming an additional E4942-H4832 interaction. When comparing different 3D reconstructions of RyR1 obtained with a variety of buffer conditions leading to a closed pore, the Mg^{2+} conditions resulted in the smallest constriction at D4945 (see Fig. 3C), providing further evidence that Mg^{2+} induces tighter association of the inner helices. Thus, Mg^{2+} occupancy of the D4945 site appears to hold the S6 helices more closely and to increase the resistance to separate and rotate counterclockwise (as seen from the cytoplasmic side) during the closed to open transition.

Stability of Mg^{2+} at the D4945 site

To elucidate the stability and dynamics of Mg^{2+} and Ca^{2+} at the central axis of the pore flanked by the carboxylate groups of D4945 from the four S6 helices, MD simulations of RyR1-ACP/LMg^{2+} (closed), RyR1-ACP/HMg^{2+} (closed), and RyR1-ACP/Ca^{2+} (open) were conducted in the presence of the divalent cations of interest, Ca^{2+} and Mg^{2+} (Table S2). In the two RyR1 closed structures, the MD trajectories revealed that Mg^{2+} remained highly stable at the D4945 site, while Ca^{2+} left the site and moved toward the cytoplasm shortly after simulation was initiated (Fig. 4A-B, D-E)—a behavior consistently reproduced (see replicas in Fig. S3). Consistent with this observation, the DFT-derived binding energies (ΔE_{bind}) in the two closed pore structures indicated a significantly higher affinity of the D4945 binding site for Mg^{2+} over Ca^{2+}, as demonstrated by the greater values for the Mg^{2+}-$D4945_4$ complex compared to the Ca^{2+}-$D4945_4$ complex (Table S3). Furthermore, the binding energy of the Mg^{2+}-$D4945_4$ complex was greater in the structure determined at high Mg^{2+} concentration compared to that determined at low Mg^{2+} concentration, aligning with the MD simulations where Mg^{2+} in the RyR1-ACP/LMg^{2+} system exhibited greater ion displacement fluctuation than Mg^{2+} in the RyR1-ACP/HMg^{2+} system. This suggests that the conformation of

bioRxiv preprint doi: https://doi.org/10.1101/2024.02.16.580716; this version posted February 21, 2024. The copyright holder for this preprint (which was not certified by peer review) is the author/funder, who has granted bioRxiv a license to display the preprint in perpetuity. It is made available under a CC-BY-NC-ND 4.0 International license.

RyR1 at the higher Mg^{2+} concentration results in allosteric effects that induce a configuration of the pore (and of D4945) with higher affinity for Mg^{2+}.

In the closed states, MD simulations illustrated that the carboxyl oxygens of D4945 engaged in hydrogen bond interactions with first-shell water molecules, establishing an indirect interaction between the cation and the protein's residues (Movies S2, S3, Fig. 5A). This arrangement implies that D4945 may serve as a second-shell ligand, contributing to the stabilization of Mg^{2+}. The role of aspartate residues serving as second-shell ligands for divalent cations is a common observation in protein structures (*30*). A hydrogen bond network involving D4945, R4944, D4938, and Mg^{2+} was observed in the RyR1/HMg^{2+}+Mg^{2+} model (Movie S3, Fig. 5B), and corresponds to the network independently identified by cryo-EM (Fig. 3B, Movie S1), highlighting the tighter packing of the cytoplasmic part of S6 helix and supporting the presence of Mg^{2+} at the D4945 site. All the above MD and DFT analyses emphasize the important role that Mg^{2+} plays in the resting state of the channel, and likely explains the malfunction of RyR1 in the presence of anomalous Mg^{2+} levels (*8, 9*). In the open conformation, D4945 did not retain Mg^{2+} or Ca^{2+} (Fig. 4C and 4F), consistent with their known permeability (*6, 31*). Thus, our MD results indicate that in the open state, the D4945 site is permeable, allowing the passage of both Mg^{2+} and Ca^{2+} ions through the channel without retention.

Mg^{2+} can occupy the high-affinity Ca^{2+} binding site without triggering activation

The Ca^{2+} activation site, at the CD/CTD interface (*17*), was empty and maximally open in the RyR1 cryo-EM map determined at low Mg^{2+}, with a conformation almost identical to that of RyR1-ACP/EGTA. At 10-fold higher free Mg^{2+} concentration and in the absence of Ca^{2+}, a clear density visible up to 7σ appeared within the Ca^{2+} activation site (CAS), which indicates binding of Mg^{2+} (Fig. 6). Mg^{2+} interacted with E3967 and Q3970 (from the CD) within its first coordination shell, and with E5002 (from the CTD) through its hydration shell. When considering the angle between the line passing through the Ca^{2+}-sensing residues of the CD (E3893, E3967, and Q3970) and the axis of the closest CTD α-helix (residues 5005-5016), the angle decreased by ~2°. This is a small "pull" when compared to the ~15° angle closure produced by Ca^{2+} activation (measured in two open states (PDB ID: 5TAL (*17*) and PDB ID: 7TDH (*26*)), in agreement with the inability of Mg^{2+} to activate the channel. Comparison of the RyR1 structures obtained in the presence of Ca^{2+} and HMg^{2+} revealed that both divalent cations interact with E3967, but Mg^{2+} interacts with Q3970 instead of E3893, and with E5002 instead of the carbonyl of T5001 (Fig. 6, Fig. S4, Movie S4). Thus, the CD pivots either leaving the cavity more open on its N' terminus in the presence of Mg^{2+} or more open on its C' terminus in the presence of Ca^{2+}. Overall, mainly through side chain reorientation of the CD and CTD residues, Mg^{2+}'s coordination stabilizes the interaction between the CD and CTD domains, but the partly hydrated Mg^{2+} appears to act as a spacer between them, pushing the CTD down and stabilizing the CAS in the position characteristic of the closed state.

Conformational change of the EF-hand domain at high Mg^{2+}

The EF hand domain, spanning amino acids 4071-4131, forms a distinctive globular shape protruding from the cytoplasmic assembly via its two flanking helices: the incoming α-helix emerges from the CD, and the outgoing α-helix goes to the U-motif. The EF hand domain has two helix-loop-helix modules, where the EF1 and EF2 loops have negative charges that can bind Ca^{2+}

bioRxiv preprint doi: https://doi.org/10.1101/2024.02.16.580716; this version posted February 21, 2024. The copyright holder for this preprint (which was not certified by peer review) is the author/funder, who has granted bioRxiv a license to display the preprint in perpetuity. It is made available under a CC-BY-NC-ND 4.0 International license.

with low affinity (*32*). At low Mg^{2+}, the position of the EF-hand domain of RyR1 resembles that observed in the presence of EGTA. However, at high Mg^{2+} concentration the EF-hand rotated towards the 122-residue long cytoplasmic loop between the S2 and S3 transmembrane helices of the neighboring subunit. Specifically, residues E4075 and K4101 from the EF hand domain were within salt bridge distance of residues R4736 and D4730 of the S2-S3 loop, respectively (Fig. 7A, panel ACP/HMg^{2+}, Fig. 7B). This configuration is almost identical to that found for Ca^{2+}-inactivated RyR1 (Fig. 7A, panel ACP/HCa^{2+} inactivated) (*26*). RyR1 in the open conformation (*17, 26*) also shows approximation of the EF hand domain and S2-S3 loop, but the two domains are more separated (Fig. 7A, panels ACP/HCa^{2+} open and ACP/LCa^{2+}/caff open) than in the inactivated conformation. Ca^{2+} was not resolved within the EF hand domain of Ca^{2+}-inactivated RyR1 or any other RyR1 structure in the presence of Ca^{2+}, and no coordinated metal is resolved at high Mg^{2+} either, largely due to the low resolution of this domain that hampers precise modeling of the main chain or visualization of any metal bound. Potential reasons for the low resolution of the EF hand domain could be fractional occupancy of the site by cation(s) leading to coexistence of conformations, and that this domain protrudes from the cytoplasmic domain allowing higher mobility.

Another possible explanation for the conformational change observed in the EF hand domain is that binding of divalent cations to the CAS in the CD domain could induce repositioning of the EF hands, since the CD and EF hand domains are connected (Fig. 7C). However, given that the translation of the EF hand domain (~10 Å) is much larger than the translation of the connected domains (less than 2 Å for the CD and U-motif) and that the EF hand domain only moves in the presence of Ca^{2+} or high Mg^{2+}, metal chelation seems the major mechanism to account for the reorientation of the EF hand domain. In the canonical mechanism of Ca^{2+} sensing, chelation of divalent cations by the helix-loop-helix motifs of the EF hands changes the angle between such helices, which is also obvious in RyR1's EF hands (Fig. 7D). Reorientation of RyR1's EF hands at high Ca^{2+} or Mg^{2+} also resulted in detachment of the incoming α-helix (residues 4053-4070) from the CD (see Fig. 7A and Movie S4), further corroborating that the conformational change in the EF hand domain forced reorientation of its N' terminus with respect to its C' terminus. The immobility of the outgoing α-helix suggests higher rigidity of the U-motif.

Our results indicate that the EF hand domain of RyR1 can sense both Ca^{2+} and Mg^{2+}. Considering that micromolar Ca^{2+} induced more movement in the EF hand than 1 mM Mg^{2+} (compare Fig. 7A, top left and bottom right panels) reflects a higher affinity of the EF hand domain for Ca^{2+} than for Mg^{2+}. We propose that this site, shared by both Mg^{2+} and Ca^{2+}, may correspond to a hypothesized inhibitory divalent sensor, where activation of this sensor adds an additional interaction between neighboring subunits (Fig. 7B).

Mg^{2+} lodges within the ATP binding site

ATP binds to a pocket formed by the U-motif, S6C', and CTD within the same subunit (*17*). The S6C' and CTD constitute the innermost portion of the binding pocket that houses the nucleotide base moiety, whilst the U-motif contributes binding to the distal triphosphate tail (Fig. 8A). Presence of Mg^{2+} resulted in a conspicuous larger mass around the ACP triphosphate moiety, which was well resolved in the RyR1-ACP/HMg^{2+} map. Two putative densities could be attributed to Mg^{2+}; one of them forms a bidentate complex with oxygens in the α and γ phosphate, and the

bioRxiv preprint doi: https://doi.org/10.1101/2024.02.16.580716; this version posted February 21, 2024. The copyright holder for this preprint (which was not certified by peer review) is the author/funder, who has granted bioRxiv a license to display the preprint in perpetuity. It is made available under a CC-BY-NC-ND 4.0 International license.

other connects with the oxygens of the phosphate backbone (Fig. 8B). Overall, Mg^{2+} triggered clockwise in-plane rotation (as seen from the cytoplasmic side) of the S6C'-U-motif region, drawing the ACP molecule into the cavity in a concentration-dependent manner. The U-motif, which is close to the phosphate tail in RyR1-ACP and RyR1-ACP/LMg^{2+} due to interactions via K4211, K4214, and R4215, is separated (by 10 Å) from the phosphate tail and forms an extra contact with the CTD (H4983) in RyR1-ACP/HMg^{2+}, similar to the Ca^{2+}-inactivated structure that stabilizes an inward-drawn conformation of the nucleotide base. It appears that the nucleotide settling deeper into its binding pocket is more a consequence of the conformational rearrangement caused by coordination of Mg^{2+} at other sites of the channel than a direct consequence of Mg^{2+} binding to the nucleotide.

The lipid-binding pocket in the TMD is occupied

The domain-swapped inter-subunit space of RyR1-ACP/HMg^{2+}, formed by S3/S4 and S5/S6 of the neighboring subunit, was occupied by non-protein densities identified as two molecules of phosphatidylcholine (PC16:0/18:1), based on the addition of this lipid during reconstitution into nanodiscs and the cryo-EM densities for their head group (Fig. S5). Lipid-1 primarily interacts with six amino acids at S5/S6, while lipid-2 interacts with twelve amino acids at S3/S4 (Fig. 9). Together, the lipid buries 783 $Å^2$ of the cavity lined by hydrophobic side chains of S3, S4, S5, and S6. The configuration of the lipid moiety and surrounding pocket is practically identical to that found in closed RyR1 structures solved in the presence of lipids, e.g., RyR1-ACP/Ca^{2+}-inactivated (PDB ID: 7TDG (*26*)), Y522S RyR1 closed (PDB ID: 7T64 (*33*)), RyR1-FKBP bound closed (PDB ID: 7TZC (*34*)), as well as closed RyR2 R176Q (PDB ID: 6WOU (*25*)), with more of the head and fatty acyl tail of lipid-2 resolved in RyR1-ACP/HMg^{2+}. As mentioned earlier, lipid-2 forms a steric clash with S4 of open channels (*26*), which supports the participation of lipids in RyR's gating transitions.

Discussion

We carried out functional, structural, and molecular dynamics studies to understand RyR1 inhibition by Mg^{2+}. The structural analysis of pure RyR1 particles in the vitrified state was obtained in the presence of the cytosolic modulators Mg^{2+} and an ATP analog. The use of nanodiscs to preserve the transmembrane domains in a detergent-free manner provided a lipidic environment with millimolar concentrations of Mg^{2+} and ATP as representative as possible of the native resting closed state of the RyR1. In a second reconstruction, we used a 10-fold free Mg^{2+} concentration range to enable higher binding site saturation and help resolve ion occupancy. Using high-resolution cryo-EM and MD, we identified putative Mg^{2+} binding sites and characterized the effect of Mg^{2+} on RyR1's conformation. Based on the observations reported here, we propose a multi-factorial mechanism of inhibition by Mg^{2+}.

A main inhibitory effect of Mg^{2+} derives from its binding to the pore by coordinating the four inner helices along the ion permeation pathway. This coordination site is provided by the four D4945 residues in the cytoplasmic portion of S6. The side chains of D4945 extend towards the center, in contrast to RyR1 without Mg^{2+} where such side chains are tucked (see Fig. 3). At the center of the extended side chains there is a self-standing mass attributed to Mg^{2+}, which increases in density at

bioRxiv preprint doi: https://doi.org/10.1101/2024.02.16.580716; this version posted February 21, 2024. The copyright holder for this preprint (which was not certified by peer review) is the author/funder, who has granted bioRxiv a license to display the preprint in perpetuity. It is made available under a CC-BY-NC-ND 4.0 International license.

the higher Mg^{2+} concentration. MD and DFT calculations validated that D4945 in the inner helices can accommodate Mg^{2+} but not Ca^{2+}, and that coordination with Mg^{2+} occurs exclusively in the closed conformation (Fig. 4A, B). At 10 mM free Mg^{2+}, the axial density attributed to Mg^{2+} near D4945 is well defined, with a density of 6σ matching that of surrounding residues. MD substantiates that the side chains of D4945 engage in hydrogen bonds with the first shell of hydration of Mg^{2+} (Fig. 5). Thus, our results from cryo-EM and MD together suggest that D4945 in the inner helices constitute a binding site for Mg^{2+} along the closed ion pathway. Coordination of Mg^{2+} to the inner helices was less favorable in the open conformation (Fig. 4C), supporting the fact that Mg^{2+} permeates the activated channel and plays a role in inhibition by competing for ion flow, in agreement with functional data (*6, 21, 23*).

An obvious difference between the 3D reconstructions of RyR1-ACP/Mg^{2+} and RyR1-ACP/EGTA is an extra density in the vicinity of the known ATP binding site (Fig. 8). This implies that under physiological conditions, it is Mg^{2+}-ATP (not ATP alone) that binds within the U-motif/S6/CTD cavity. Mg^{2+} likely increases the structural continuity between domains by filling up the cavity. Considering that ATP is indispensable for skeletal-type EC coupling (*8*), reducing flexibility at this interface probably increases the efficiency in the long-range allosteric relay of the signal from the DHPR to RyR1's ion gate. Because ATP is an activator and Mg^{2+} enhances the ATP interaction with RyR1, it appears that as suggested earlier, ATP exerts its activating effect on the channel in complex with Mg^{2+} (*7*).

The cryo-EM density map shows that Mg^{2+} occupies the high affinity Ca^{2+} activation site in a concentration-dependent manner. At 1 mM free Mg^{2+}, the high affinity Ca^{2+} binding site is empty, while at 10 mM free Mg^{2+} the cation lodged into the high affinity Ca^{2+} binding site (Fig. 6). The ionic strength used in the cryo-EM experiments (0.635 M KCl) was higher than physiological, decreasing the affinity of Mg^{2+} to this site (*22*). Thus, most likely, at physiological ionic strength, the CAS site should be at least partially occupied by 1 mM Mg^{2+}. Even if both cations compete for the same site, owing to their different coordination properties they induce different effects in the CD/CTD interaction: Ca^{2+} binding induces closure of the CAS cavity (i.e., approximation of the CD and CTD domains; Fig. S4) which leads to opening of the ion gate (*17*), while the larger hydrated Mg^{2+} keeps the CAS cavity in an open configuration, similar to that adopted in the absence of Ca^{2+} (RyR1-ACP/EGTA) (Fig. 6) where the ion gate is closed. Thus, presence of Mg^{2+} at the cavity stabilizes an orientation of the CTD that keeps the inner helices of RyR1 in the closed state.

It was suggested that one of the mechanisms of Mg^{2+} inhibition could be competition for the high affinity Ca^{2+} binding site (*7, 8, 20, 21*). Ca^{2+} occupancy of its high affinity cavity is in the μM range, whereas Mg^{2+}'s is in the mM range; implying at least a 1,000-fold higher affinity of Ca^{2+} versus Mg^{2+} for the site. This relative affinity between Mg^{2+} and Ca^{2+} corresponds approximately to the relative free concentrations of the two cations in the cytoplasm of skeletal muscle during activation, revealing a fine-tuning of the CAS site to the ratio between both divalent cations in the cytoplasm and supporting an inhibitory role of Mg^{2+} at rest (i.e., sub μM free Ca^{2+} concentration). The antagonistic action of Mg^{2+} would be easily overcome as cytoplasmic Ca^{2+} increases. Mg^{2+} occupancy at this site can also explain the inability to trigger EC coupling at 10 mM free Mg^{2+}, concentration at which Ca^{2+} competition may be unfavorable (*8, 9*).

We described an inactivated conformation of RyR1 at high (inactivating) Ca^{2+} concentration, with Ca^{2+} bound to the CAS while the pore is closed (*26*). There is a noticeable difference between the Mg^{2+}-inhibited and the 2 mM Ca^{2+}-inactivated state. Compared to the tightly closed CAS cavity

bioRxiv preprint doi: https://doi.org/10.1101/2024.02.16.580716; this version posted February 21, 2024. The copyright holder for this preprint (which was not certified by peer review) is the author/funder, who has granted bioRxiv a license to display the preprint in perpetuity. It is made available under a CC-BY-NC-ND 4.0 International license.

in the 2 mM Ca^{2+}- inactivated state, the CAS cavity is open when occupied at high Mg^{2+} concentration (see Fig. 6B, two middle panels), which could have the opposite function, to facilitate exchange with Ca^{2+} by keeping the CD/CTD domains separated. Thus, high Ca^{2+} inactivates the channel preventing further activation, while Mg^{2+} inhibits the channel leading to a conformation of the CAS site more ready to be activated.

In the presence of divalent cations, the EF hand domain of RyR1 moves towards the cytoplasmic S2-S3 loop of the neighboring subunit (Fig. 7). While the conformational change induced by CAS occupancy in the close vicinity may help positioning the EF hand domain, the movement of the EF hand is of larger magnitude, suggesting direct interaction of the cation at the EF hand loop(s). This was well documented for the activated conformation induced by μM Ca^{2+} , showing rotation and translation of the EF hand with respect to the CD (9.7º and 6.2 Å versus 2.9º and 1.3 Å, respectively) (*33*). In the inactivated conformation induced by mM Ca^{2+} the EF hand domain moved further (Fig. 7A), with two salt bridges between the two domains joining two adjacent RyR1 subunits and presumably stabilizing the non-conductive conformation of the pore (*26*). The important role of the two putative salt bridges was supported by three human disease mutations characterized by inactivation-deficient channels (*35*), where these mutations would hamper the interaction between the EF hand and the S2-S3 loop. The Ca^{2+}-sensing ability of the EF hand domain of RyR1 was also shown before, where scrambling the negatively charged residues within the EF1 loop reduced the sensitivity of the channel to Ca^{2+}-induced inactivation (*36*). In the presence of 10 mM free Mg^{2+} the EF hand domain of RyR1 moved towards the cytoplasmic S2-S3 loop of the neighboring subunit almost to the same extent than in the presence of 2 mM Ca^{2+} (Fig. 7A), suggesting that the EF hand domain may correspond to a predicted low-affinity inhibitory site shared between Ca^{2+} and Mg^{2+} (*7, 16, 20*).

As Mg^{2+} is always present in the cell, it necessitates an explanation of how its inhibition is released. In skeletal muscle the T-tubules, invaginations of the plasma membrane, bring the voltage gated L-type Ca^{2+} channel ($Ca_V1.1$ or DHPR) into very close contact with the RyR1, making for efficient conformational coupling between the two proteins and bringing about RyR1-mediated Ca^{2+} release and muscle contraction as a response to a nervous impulse (*37-39*). Studies of the influence of Mg^{2+} showed a strong effect of its concentration on EC coupling in skinned skeletal muscle fibers. At 1 mM free Mg^{2+}, the muscle fibers were quiescent, and only DHPR activation could overcome Mg^{2+} inhibition, leading to RyR1 channel opening (*8, 9*). Lowering the concentration of Mg^{2+} 10-fold triggered massive spontaneous Ca^{2+} release, while a 10-fold increase of Mg^{2+} abrogated depolarization-induced Ca^{2+} release (*8, 9, 14*). This, among other findings, led to the hypothesis that DHPR activates the RyR1 by removing the potent inhibitory effect of Mg^{2+} at its physiological concentration of 1 mM (*13*). In other words, activation of the DHPR would decrease the affinity of RyR1 for Mg^{2+}, which would account for Ca^{2+} release upon depolarization.

Our structural work mirrors these functional findings and provides strong structural basis for the DHPR-control of Mg^{2+} inhibition. We suggest that unlocking the S6 helical bundle is triggered by conformational coupling to DHPR, which would then abrogate the effect of the electrostatic network coordinating Mg^{2+}. This leaves the question of how the DHPR effects such change in S6. One potential mechanism is via a ~100 Å-long lever that spans from the DHPR-facing region of RyR1 to the base of the CD (Fig. 10) that abates its angle by 6º when RyR1 is stimulated with Ca^{2+} (*33*). It is likely that this lever forms part of the long-range allosteric pathway connecting DHPR and RyR1's channel, as a severe RyR1 disease mutation in the DHPR-facing region of the lever abated the angle of this lever by 5º under closed-state conditions (*33*) and increased the sensitivity

bioRxiv preprint doi: https://doi.org/10.1101/2024.02.16.580716; this version posted February 21, 2024. The copyright holder for this preprint (which was not certified by peer review) is the author/funder, who has granted bioRxiv a license to display the preprint in perpetuity. It is made available under a CC-BY-NC-ND 4.0 International license.

of DHPR to depolarization by 40 mV (*40*). Thus, the change in the DHPR voltage sensor upon depolarization, potentially moving (abating) the long levers of RyR1, could constitute a mechanism to directly induce a separation of the inner helices, disrupting the Mg^{2+} coordination and unblocking the channel.

As mentioned earlier, free Mg^{2+} concentration of 10 mM abrogated depolarization-induced Ca^{2+} release (*8, 9*). We find two sites that get occupied at high Mg^{2+} but not low Mg^{2+}: the high affinity Ca^{2+} binding site and EF-hand domain. Fractional occupancy must start somewhere between the two Mg^{2+} concentration studied, with the full occupancy observed here at 10 mM free Mg^{2+} probably corresponding to a lower concentration at physiological ionic strength (*16, 41*). This suggests that Mg^{2+} may operate at these two sites under physiological conditions, creating an inhibited conformation of RyR1. In addition, coordination of the inner helices by Mg^{2+} may translate into stability of the closed conformation of RyR1 and resistance against reversible activation by DHPR.

In sum, we posit that Mg^{2+} can inhibit the RyR1 by binding at the following different sites of RyR1: (a) the high affinity Ca^{2+} activation site, where given its larger hydrated radius would keep the cavity in a "dormant" but Ca^{2+}-accessible conformation, (b) the EF hand domain, changing its orientation and priming it to form salt bridges with the neighboring subunit, and (c) the pore domain, coordinating the four inner helices in the closed conformation (see summary in Fig. 10). In the EC coupling mechanism, the depolarization-activated DHPR activates its physically coupled RyR1s. We suggest that this action would increase separation of the S6 helices, at which point Mg^{2+} would lose the coordination to S6, allowing Ca^{2+} (and Mg^{2+}) permeation. Ca^{2+} would then bind to the high affinity site further activating the channel and subsequently, the Ca^{2+} released into the cytoplasm would start to inactivate the channel limiting Ca^{2+} release. In the absence of membrane depolarization, DHPR has an inhibitory effect on RyR1 (*42-44*). Thus, after skeletal muscle excitation ends and DHPR ceases to be activated, the inner helices of RyR1 would return to the closed conformation under direct action of the DHPR and recover their ability to coordinate Mg^{2+}.

Materials and Methods

Reagents

All chemicals were purchased from Thermo Fisher Scientifc or Sigma-Aldrich except where indicated.

Purification of rabbit skeletal muscle RyR1

Sarcoplasmic reticulum (SR) membranes were purified from rabbit back muscles through differential centrifugation as previously described (*29*). 100 mg frozen membranes were thawed and solubilized in 10 ml of buffer-A containing 20 mM MOPS pH 7.4, 1 M NaCl, 9.2% (w/v) CHAPS, 2.3% (w/v) Phosphatdylcholine (PC; Sigma), 2 mM DTT and protease inhibitor cocktail with constant stirring for 15 mins at 4 ^{o}C. The solubilized membranes were centrifuged at 100,000 x g for 60 min and the pellet was discarded. Supernatant was layered onto a 10-20% (w/v) discontinuous sucrose gradient. Gradient was prepared in buffer-A containing 0.5% CHAPS and

bioRxiv preprint doi: https://doi.org/10.1101/2024.02.16.580716; this version posted February 21, 2024. The copyright holder for this preprint (which was not certified by peer review) is the author/funder, who has granted bioRxiv a license to display the preprint in perpetuity. It is made available under a CC-BY-NC-ND 4.0 International license.

0.125% PC (buffer-B). The layered sucrose gradient tubes were ultracentrifuged at 141,000 x g for ~20 h at 4 ºC to allow RyR1 separation. Fractions containing >95% pure RyR1 were pooled and further purified with HiTrap Heparin HP Agarose column (GE Healthcare), after a five-fold dilution step. RyR1 was eluted with buffer B containing 0.635 M KCl after washing with 20 column volumes of buffer B with 200 mM KCl. Peak fractions were flash-frozen and stored at -80 ºC until nanodisc reconstitution and cryo-EM. 1.5-2 mg of RyR1 was purified from 100 mg of SR vesicles. RyR1 purity was estimated with 12.5% SDS-PAGE and negative staining with 0.75% Uranyl formate. Total protein concentration in purified microsomes and RyR1 fractions was measured with Quick Start Bradford Protein Assay (Bio-Rad).

[^{3}H]Ryanodine binding

RyR1 activity was estimated by measuring the extent of bound [^{3}H]ryanodine in SR membrane vesicles isolated from rabbit skeletal muscle when incubated with free Ca^{2+} (100 nM to 2 mM range) alone or in the presence of 1 mM free Mg^{2+}, 2 mM ATP, or 5 mM ATP-Mg^{2+}. Effect of free Mg^{2+}, ATP-Mg^{2+} and ATP on activated RyR1 was studied by incubation of SR membrane vesicles with 50 µM $CaCl_2$ in the presence of 1 µM-5 mM $MgCl_2$, ATP-Mg^{2+} or ATP [1 µM-5 mM]. Concentrations of total divalent ion to be added to the reaction mixture were estimated in Maxchelator (*45*). Preincubated membrane vesicles (30-40 µg) were allowed to bind 5 nM [^{3}H]ryanodine (PerkinElmer) in a buffer containing 50 mM MOPS (pH 7.4), 0.15 M KCl, 0.3 mM EGTA, protease inhibitors, and 2 mM DTT for 1 h at 37ºC. Aliquots of samples were diluted seven-fold with an ice-cold wash buffer (0.15 M KCl) before placing onto Whatman GF/B filter papers in a vacuum operated filtration apparatus. The radioactivity remaining in filter papers after washing three times with the wash buffer was estimated by liquid scintillation counting. Non-specific ryanodine binding was estimated in the presence of 25 µM unlabeled ryanodine (Tocris) and subtracted from the total binding. Data represent the mean specific [^{3}H] ryanodine binding for three independent experiments.

Reconstitution of RyR1 into nanodiscs

Reconstitution into nanodiscs was carried out as indicated previously (*25*). Briefly, the plasmid pMSP1E3D1 (Addgene) encoding for MSP1E3D1 was expressed in *E.coli* and purified using the manufacturer's instructions. RyR1-nanodiscs were obtained by mixing purified RyR1, MSP1E3D1 and POPC (Avanti polar lipids) at a 1:2:50 molar ratio. The mixture was incubated for 1 hour 30 mins at 4º C before overnight dialysis in a CHAPS-free buffer (20 mM MOPS pH 7.4, 0.635 M KCl, 2 mM DTT) containing 5 and 11.6 mM $MgCl_2$ in case of ACP/LMg^{2+} and ACP/HMg^{2+} respectively. In the ACP condition, 1 mM EGTA and 1 mM EDTA were maintained. Maxchelator was used to compute free Mg^{2+}. The channels' integrity was confirmed using negative staining prior to cryo-EM.

Cryo-EM grid preparation and data acquisition

Cryo-EM grids were cleaned with a customized protocol (*46*) prior to glow-discharge. The dialyzed RyR1-nanodisc preparations were incubated for 30 minutes with either 5 mM ACP/5 mM Mg^{2+} (~1 mM free Mg^{2+}; ACP/LMg^{2+} dataset) or with 1 mM ACP/ 11.6 mM Mg^{2+} (~10 mM free Mg^{2+}; ACP/HMg^{2+} dataset) before being plunge frozen. Aliquots of 1.25 – 1.5 ul RyR1-nanodisc

bioRxiv preprint doi: https://doi.org/10.1101/2024.02.16.580716; this version posted February 21, 2024. The copyright holder for this preprint (which was not certified by peer review) is the author/funder, who has granted bioRxiv a license to display the preprint in perpetuity. It is made available under a CC-BY-NC-ND 4.0 International license.

were applied onto each side of glow-discharged C-Flat - 2/1 - 3Au holey-carbon (Protochips, NC) or UltraAufoil -1.2/1.3 holey-gold (Quantifoil, Germany) with 300 TEM mesh. The grids were blotted with Whatman 540 filter paper for 1-1.5 s in a Vitrobot^{TM} Mark IV (Thermo Fisher Scientific) and rapidly plunged into liquid ethane. The sample quality was initially assessed on a Tecnai F20 (Thermo Fisher Scientific) electron microscope. CryoEM data was collected in multiple sessions on a Titan Krios transmission electron microscope (Thermo Fisher Scientific) operated at 300 kV under super-resolution (RyR1-ACP/LMg^{2+}) or counting mode (RyR1-ACP/HMg^{2+}), with a K2 or K3-Summit detector (Gatan) as shown in Table S1. A Gatan Quantum Energy Filter (GIF) with a slit width of 20 eV was employed in all three datasets. Datasets were collected in automated mode with the Latitude program (Gatan) with a total electron dosage of 60 -70 $e^{-}/Å^{2}$ applied across 50-60 frames. Table S1 summarizes the image acquisition parameters.

Single-Particle Image Processing

Gain-reference normalization, frame alignment, dose-weighting and motion correction of the collected movie stacks was carried out with Motioncor2 (*47*) or patch motion correction employed in cryosparc 3.2. Contrast transfer function parameters were estimated from non-dose weighted motion corrected summed images using CTFFIND 4.0 (*48*) or Gctf (*49*). All subsequent image processing operations were carried out using dose-weighted, motion-corrected micrographs in RELION 3.0 or cryosparc3.2 (*50*). 2D class average templates for autopicking were generated by reference-free 2D classification of 1000 manually picked particles. Autopicked particles with ethane and hexagonal ice-contaminated areas and junk particles were removed prior to 2D-classification. Particle image stacks required for the reconstructions focused on domains spanning from CD to TMD (residues 3668-5037) and quarter (one-fourth) sub-volumes of RyR1 were generated using a signal subtraction procedure (employed in relion_project) which was combined with symmetry expansion (*51*) for the one-fourth sub-volume with relion_particle_symmetry_expand tool. The reported resolutions of the cryo-EM maps are based on FSC=0.143 criterion (*52*). Local resolution was estimated with ResMap (*53*). Pixel size calibration of post-processed EM maps of the datasets were carried out using real space correlation metric of UCSF Chimera (*54*) using a published RyR1 cryo-EM map (*17*). Pixel size maxima of 1.36 and 0.86 Å, were obtained for RyR1-ACP/LMg^{2+} and RyR1-ACP/HMg^{2+}, respectively. Two datasets collected under identical imaging conditions for the RyR1-ACP/LMg^{2+} were merged after a real space calibration test. Image processing schemes are summarized in Figs. S1 and S2.

Identification of the Mg^{2+} density in the ATP binding cavity

Cryo-EM map and model of RyR1-ACP/Mg^{2+} were aligned and resampled to the RyR1-ACP/EGTA map with Fit in map and vop resample tools in UCSF Chimera, respectively. Localized maps around the ATP molecule were calculated by extracting 3D-density boxes with a selection radius 10 Å from the ACP using Phenix Map Box tool (*55*). Difference maps in real space for the localized regions of RyR1 were calculated with the vop subtract tool in UCSF Chimera.

bioRxiv preprint doi: https://doi.org/10.1101/2024.02.16.580716; this version posted February 21, 2024. The copyright holder for this preprint (which was not certified by peer review) is the author/funder, who has granted bioRxiv a license to display the preprint in perpetuity. It is made available under a CC-BY-NC-ND 4.0 International license.

Model Building and Structure refinement

The cryo-EM based atomic model of RyR1-ACP/EGTA (PDB ID: 7K0T) was taken as the initial model for model building. Using the Chimera Fit in map tool, the best resolved EM map from the relevant dataset was docked with a RyR1 tetramer. An iterative approach of amino acid fitting was used to enhance the local density fit of a protomer in Coot (*56*), which was alternated with real space refinement in PHENIX (*57*). Real space refinement was carried out with secondary structure and Ramachandran restraints. The consensus reconstructions were used to assemble the tetramer models before real space refinement with NCS restraints. Comprehensive model validation of the models was carried out with Phenix.

Pore radius calculation

Pore radius measurements were carried out with the refined atomic model coordinates of the RyR1 pore region (residues 4821-5037) with the HOLE program (*58*). Dot-surfaces representing the channel ion permeation pathway were generated with HOLE (implemented in Coot) and reformatted (to .bld files) that enabled visualization in UCSF chimera.

Molecular Dynamics Simulations

To further investigate the interactions between various cations and the protein in alignment with our experimental findings, we conducted all-atom molecular dynamics (MD) simulations in explicit solvent. Structural models for RyR1/LMg^{2+}, RyR1/HMg^{2+} and RyR1/Ca^{2+} were constructed based on cryo-EM structures (PDB IDS: 7K0S, 7UMZ, 7TDH, respectively) encompassing residues in the pore domain including S5, pore helix, selectivity filter, and S6 (residues 4835-4956). The protonation states of ionizable residues (Lys, Arg, Asp and Glu) at neutral pH were assigned according to the pK_a prediction using the PROPKA software (*59*). Each model was embedded in a pre-equilibrated 1-Palmitoyl-2-Oleoyl-sn-Glycero-3-Phosphocholine (POPC) lipid environment to mimic experimental conditions and solvated with TIP3P water (*60*). Counterions were added to neutralize the overall charge of the systems, and a salt concentration of 0.6 M KCl was maintained using VMD's Autoionize plugin (*61*).

Model systems 1-6 were designed to assess the stability of the putative cation identified in the D4945 site under different structural states. In models 1, 2 and 3, hexahydrated Mg^{2+} was placed at the position dictated by the coordinates of the point of highest density within the pore axis in the cryo-EM structure of RyR1-ACP/HMg^{2+}. To compare to another common divalent cation, Mg^{2+} was replaced with heptahydrated Ca^{2+} in models 4, 5, and 6. We employed enhanced force field parameters and topology of a hydrated form of Mg^{2+} and Ca^{2+} as developed by Yoo and Aksimentiev (*62*). A summary of the simulation systems is shown in Table S2.

All-atom MD simulations were carried out with periodic boundary conditions. A distance cutoff of 12 Å was used for calculating non-bonded interactions. Electrostatic interactions were calculated with particle mesh Ewald summation via fast Fourier transform, including van der Waals interactions, with a switching distance of 10 Å. Langevin dynamics at a constant temperature of 298 K was used with a damping coefficient of 1 ps^{-1}. The pressure was kept constant at 1 atm using the Nose´−Hoover Langevin piston method, with a piston period of 200 fs and a damping time of 50 fs. Energy minimization was performed to remove bad contacts between

bioRxiv preprint doi: https://doi.org/10.1101/2024.02.16.580716; this version posted February 21, 2024. The copyright holder for this preprint (which was not certified by peer review) is the author/funder, who has granted bioRxiv a license to display the preprint in perpetuity. It is made available under a CC-BY-NC-ND 4.0 International license.

atoms. Restrained MD simulations were employed to relax structural strains of the model systems. In the first stage, the protein and the cation were initially kept fixed to their initial positions while water, lipid and counterion were allowed to equilibrate for about 1 ns. Then, the systems were equilibrated by 1 ns MD simulations with position restraints of protein atoms and the cation. During this step, a harmonic potential of force constant decreases from 1 to 0.1 kcal/(mol $Å^2$). Subsequently, MD simulations were performed for each system under NPT ensemble. To compensate for possible edge effects of the truncated regions in the model, a softness in the restraints was applied to Cα atoms of the protein of the last four residues of the N- and C-termini. The CHARMM36 force field parameter sets (*63*) were applied for protein, lipid and counterions. The simulated systems were constructed using TCL language in VMD 1.9.3. (*61*). All simulations were carried out for 100 ns using the NAMD 2.12 software (*64*). Three independent runs of MD simulations were performed for each model system.

Analyses of MD trajectories, including hydrogen bond and ion displacement were carried out using TCL scripts in VMD. Unless otherwise specified, analysis of MD trajectories was carried out during the last 20 ns simulation. This was primarily to make sure that the systems had reached thermodynamic equilibrium and that structural features extracted from the trajectory were adequately characterized with least deviation.

Binding energy calculations from Density Function Theory (DFT)

To assess the relative stability of the metal (M) in the D4945 site, we explored the binding energy of the $[M(H_2O)_n(D4945)_4]^{2+}$ complex using a density functional theory (DFT) method. The $[M(H_2O)_n(D4945)_4]^{2+}$ models containing the four D4945 residues and the hexahydrated Mg^{2+}, $[Mg(H_2O)_6]^{2+}$, or heptahydrated Ca^{2+}, $[Ca(H_2O)_7]^{2+}$, were taken from MD snapshots of the RyR1/LMg^{2+}+Mg^{2+} and RyR1/HMg^{2+}+Mg^{2+} systems (models 1, 2, 4 and 5). We performed a single point calculation on these models using the DFT method at the B3LYP level and a 6-31+G(d,p) basis set (*65*) to determine the binding energy of the complex. The solvent effect was implicitly included using the CPCM model. The binding energies (ΔE_{bind}) were obtained according to the equation:

$$\Delta E_{bind} = E_{AB} - (E_A + E_B)$$

where E_{AB} is the energy of the $[Mg(H_2O)_6(D4945)_4]^{2+}$ or $[Ca(H_2O)_7(D4945)_4]^{2+}$ complexes, and E_A and E_B are the energies of subsystems $[Mg(H_2O)_6]^{2+}$ or $[Ca(H_2O)_7]^{2+}$ and $(D4945)_4$, respectively. Total energies of the complex (E_{AB}) and subsystems (E_A and E_B) were computed separately. Moreover, we further examined an impact of the optimized structure on the binding energy of the complex. The geometry optimization on these models was performed using the PM3 method (*66*). Subsequently, binding energy calculations on the optimized structure were carried out with the same level of theory. Convergence was achieved when the maximum force acting on any atom fell below 0.001 Hartree/Bohr. The maximum allowed displacement was set at 0.005 Å. All DFT computations were performed using the Gaussian 09 software package (*67*).

Statistical Analysis

Data are presented as means ± SEM, with the number of independent experiments indicated in the figure legends. SEMs calculated for each data point for mean specific [^{3}H] Ryanodine binding are reported. [^{3}H] Ryanodine binding data were fitted using nonlinear regression analysis in

bioRxiv preprint doi: https://doi.org/10.1101/2024.02.16.580716; this version posted February 21, 2024. The copyright holder for this preprint (which was not certified by peer review) is the author/funder, who has granted bioRxiv a license to display the preprint in perpetuity. It is made available under a CC-BY-NC-ND 4.0 International license.

Graphpad Prism 5.0. Figures were generated using PyMOL, ChimeraX, and CorelDrawX7. Movies were generated using PyMOL, ChimeraX, VMD 1.9.3, Windows Movie Maker 2012, and ffmpeg in Linux. Graphs were generated with Graphpad Prism and OriginPro 2015.

References

1. J. T. Lanner, D. K. Georgiou, A. D. Joshi, S. L. Hamilton, Ryanodine receptors: structure, expression, molecular details, and function in calcium release. *Cold Spring Harb Perspect Biol* **2**, a003996 (2010).
2. G. Meissner, The structural basis of ryanodine receptor ion channel function. *J Gen Physiol* **149**, 1065-1089 (2017).
3. M. Samso, A guide to the 3D structure of the ryanodine receptor type 1 by cryoEM. *Protein Sci* **26**, 52-68 (2017).
4. E. Rios, G. Pizarro, Voltage sensor of excitation-contraction coupling in skeletal muscle. *Physiol Rev* **71**, 849-908 (1991).
5. C. Paolini, J. D. Fessenden, I. N. Pessah, C. Franzini-Armstrong, Evidence for conformational coupling between two calcium channels. *Proc Natl Acad Sci U S A* **101**, 12748-12752 (2004).
6. D. Gillespie, H. Chen, M. Fill, Is ryanodine receptor a calcium or magnesium channel? Roles of K+ and Mg2+ during Ca2+ release. *Cell Calcium* **51**, 427-433 (2012).
7. G. Meissner, E. Darling, J. Eveleth, Kinetics of rapid Ca2+ release by sarcoplasmic reticulum. Effects of Ca2+, Mg2+, and adenine nucleotides. *Biochemistry* **25**, 236-244 (1986).
8. G. D. Lamb, D. G. Stephenson, Effect of Mg2+ on the control of Ca2+ release in skeletal muscle fibres of the toad. *J Physiol* **434**, 507-528 (1991).
9. G. D. Lamb, D. G. Stephenson, Effects of intracellular pH and [Mg2+] on excitation-contraction coupling in skeletal muscle fibres of the rat. *J Physiol* **478 (Pt 2)**, 331-339 (1994).
10. D. R. Laver, T. M. Baynes, A. F. Dulhunty, Magnesium inhibition of ryanodine-receptor calcium channels: evidence for two independent mechanisms. *J Membr Biol* **156**, 213-229 (1997).
11. D. R. Laver, B. N. Honen, Luminal Mg2+, a key factor controlling RYR2-mediated Ca2+ release: cytoplasmic and luminal regulation modeled in a tetrameric channel. *J Gen Physiol* **132**, 429-446 (2008).
12. L. Csernoch, J. C. Bernengo, P. Szentesi, V. Jacquemond, Measurements of intracellular Mg2+ concentration in mouse skeletal muscle fibers with the fluorescent indicator mag-indo-1. *Biophys J* **75**, 957-967 (1998).
13. G. D. Lamb, D. G. Stephenson, Importance of Mg2+ in excitation-contraction coupling of skeletal muscle. *NIPS* **7**, 270-274 (1992).
14. H. Westerblad, D. G. Allen, Myoplasmic free Mg2+ concentration during repetitive stimulation of single fibres from mouse skeletal muscle. *J Physiol* **453**, 413-434 (1992).
15. D. S. Steele, A. M. Duke, Defective Mg2+ regulation of RyR1 as a causal factor in malignant hyperthermia. *Arch Biochem Biophys* **458**, 57-64 (2007).
16. D. R. Laver *et al.*, Reduced inhibitory effect of Mg2+ on ryanodine receptor-Ca2+ release channels in malignant hyperthermia. *Biophys J* **73**, 1913-1924 (1997).
17. A. des Georges *et al.*, Structural Basis for Gating and Activation of RyR1. *Cell* **167**, 145-157 e117 (2016).
18. Y. Chen *et al.*, Myoplasmic resting Ca2+ regulation by ryanodine receptors is under the control of a novel Ca2+-binding region of the receptor. *Biochem J* **460**, 261-271 (2014).
19. G. G. Du, D. H. MacLennan, Ca(2+) inactivation sites are located in the COOH-terminal quarter of recombinant rabbit skeletal muscle Ca(2+) release channels (ryanodine receptors). *J Biol Chem* **274**, 26120-26126 (1999).

bioRxiv preprint doi: https://doi.org/10.1101/2024.02.16.580716; this version posted February 21, 2024. The copyright holder for this preprint (which was not certified by peer review) is the author/funder, who has granted bioRxiv a license to display the preprint in perpetuity. It is made available under a CC-BY-NC-ND 4.0 International license.

20. D. R. Laver, Regulation of the RyR channel gating by Ca(2+) and Mg(2). *Biophys Rev* **10**, 1087-1095 (2018).
21. K. Nagasaki, M. Kasai, Channel selectivity and gating specificity of calcium-induced calcium release channel in isolated sarcoplasmic reticulum. *J Biochem* **96**, 1769-1775 (1984).
22. D. R. Laver, E. R. O'Neill, G. D. Lamb, Luminal Ca2+-regulated Mg2+ inhibition of skeletal RyRs reconstituted as isolated channels or coupled clusters. *J Gen Physiol* **124**, 741-758 (2004).
23. J. S. Smith, R. Coronado, G. Meissner, Single channel measurements of the calcium release channel from skeletal muscle sarcoplasmic reticulum. Activation by Ca2+ and ATP and modulation by Mg2+. *J Gen Physiol* **88**, 573-588 (1986).
24. K. Mio, C. Sato, Lipid environment of membrane proteins in cryo-EM based structural analysis. *Biophys Rev* **10**, 307-316 (2018).
25. K. A. Iyer *et al.*, Structural mechanism of two gain-of-function cardiac and skeletal RyR mutations at an equivalent site by cryo-EM. *Science advances* **6**, eabb2964 (2020).
26. A. R. Nayak, M. Samso, Ca(2+)-inactivation of the mammalian ryanodine receptor type 1 in a lipidic environment revealed by cryo-EM. *Elife* **11**, (2022).
27. F. A. Lai, M. Misra, L. Xu, H. A. Smith, G. Meissner, The ryanodine receptor-Ca2+ release channel complex of skeletal muscle sarcoplasmic reticulum. Evidence for a cooperatively coupled, negatively charged homotetramer. *J Biol Chem* **264**, 16776-16785 (1989).
28. T. W. E. Steele, M. Samso, The FKBP12 subunit modifies the long-range allosterism of the ryanodine receptor. *J Struct Biol* **205**, 180-188 (2019).
29. M. Samso, W. Feng, I. N. Pessah, P. D. Allen, Coordinated Movement of Cytoplasmic and Transmembrane Domains of RyR1 upon Gating. *PLoS Biology* **7**, 980-995 (2009).
30. T. Dudev, Y. L. Lin, M. Dudev, C. Lim, First-second shell interactions in metal binding sites in proteins: a PDB survey and DFT/CDM calculations. *J Am Chem Soc* **125**, 3168-3180 (2003).
31. D. Gillespie, L. Xu, Y. Wang, G. Meissner, (De)constructing the ryanodine receptor: modeling ion permeation and selectivity of the calcium release channel. *J Phys Chem B Condens Matter Mater Surf Interfaces Biophys* **109**, 15598-15610 (2005).
32. H. Xiong *et al.*, Identification of a Two EF-Hand Ca2+ Binding Domain in Lobster Skeletal Muscle Ryanodine Receptor/Ca2+ Release Channel. *Biochemistry* **37**, 4804-4814 (1998).
33. K. A. Iyer, Y. Hu, T. Klose, T. Murayama, M. Samso, Molecular mechanism of the severe MH/CCD mutation Y522S in skeletal ryanodine receptor (RyR1) by cryo-EM. *Proc Natl Acad Sci U S A* **119**, e2122140119 (2022).
34. Z. Melville, K. Kim, O. B. Clarke, A. R. Marks, High-resolution structure of the membrane-embedded skeletal muscle ryanodine receptor. *Structure* **30**, 172-180 e173 (2022).
35. A. C. Gomez, T. W. Holford, N. Yamaguchi, Malignant hyperthermia-associated mutations in the S2-S3 cytoplasmic loop of type 1 ryanodine receptor calcium channel impair calcium-dependent inactivation. *Am J Physiol Cell Physiol* **311**, C749-c757 (2016).
36. J. D. Fessenden, W. Feng, I. N. Pessah, P. D. Allen, Mutational analysis of putative calcium binding motifs within the skeletal ryanodine receptor isoform, RyR1. *J Biol Chem* **279**, 53028-53035 (2004).
37. E. Rios, G. Brum, Involvement of dihydropyridine receptors in excitation-contraction coupling in skeletal muscle. *Nature* **325**, 717-720 (1987).
38. T. Tanabe, K. G. Beam, J. A. Powell, S. Numa, Restoration of excitation-contraction coupling and slow calcium current in dysgenic muscle by dihydropyridine receptor complementary DNA. *Nature* **336**, 134-139 (1988).
39. J. Nakai *et al.*, Enhanced dihydropyridine receptor channel activity in the presence of ryanodine receptor. *Nature* **380**, 72-75 (1996).
40. G. Avila, R. T. Dirksen, Functional effects of central core disease mutations in the cytoplasmic region of the skeletal muscle ryanodine receptor. *J Gen Physiol* **118**, 277-290 (2001).

bioRxiv preprint doi: https://doi.org/10.1101/2024.02.16.580716; this version posted February 21, 2024. The copyright holder for this preprint (which was not certified by peer review) is the author/funder, who has granted bioRxiv a license to display the preprint in perpetuity. It is made available under a CC-BY-NC-ND 4.0 International license.

41. G. Meissner, E. Rios, A. Tripathy, D. A. Pasek, Regulation of skeletal muscle Ca2+ release channel (ryanodine receptor) by Ca2+ and monovalent cations and anions. *J Biol Chem* **272**, 1628-1638 (1997).
42. J. M. Eltit *et al.*, Orthograde dihydropyridine receptor signal regulates ryanodine receptor passive leak. *Proc Natl Acad Sci U S A* **108**, 7046-7051 (2011).
43. J. Zhou *et al.*, A probable role of dihydropyridine receptors in repression of Ca2+ sparks demonstrated in cultured mammalian muscle. *Am J Physiol Cell Physiol* **290**, C539-553 (2006).
44. G. Robin, B. Allard, Dihydropyridine receptors actively control gating of ryanodine receptors in resting mouse skeletal muscle fibres. *J Physiol* **590**, 6027-6036 (2012).
45. D. M. Bers, C. W. Patton, R. Nuccitelli, A practical guide to the preparation of Ca(2+) buffers. *Methods Cell Biol* **99**, 1-26 (2010).
46. L. A. Passmore, C. J. Russo, Specimen Preparation for High-Resolution Cryo-EM. *Methods Enzymol* **579**, 51-86 (2016).
47. S. Q. Zheng *et al.*, MotionCor2: anisotropic correction of beam-induced motion for improved cryo-electron microscopy. *Nature Methods* **14**, 331-332 (2017).
48. A. Rohou, N. Grigorieff, CTFFIND4: Fast and accurate defocus estimation from electron micrographs. *J Struct Biol* **192**, 216-221 (2015).
49. K. Zhang, Gctf: Real-time CTF determination and correction. *J Struct Biol* **193**, 1-12 (2016).
50. S. H. Scheres, RELION: implementation of a Bayesian approach to cryo-EM structure determination. *J Struct Biol* **180**, 519-530 (2012).
51. X.-c. Bai, E. Rajendra, G. Yang, Y. Shi, S. H. W. Scheres, Sampling the conformational space of the catalytic subunit of human γ-secretase. *eLife* **4**, e11182 (2015).
52. S. H. W. Scheres, S. Chen, Prevention of overfitting in cryo-EM structure determination. *Nature Methods* **9**, 853-854 (2012).
53. A. Kucukelbir, F. J. Sigworth, H. D. Tagare, Quantifying the local resolution of cryo-EM density maps. *Nat Methods* **11**, 63-65 (2014).
54. E. F. Pettersen *et al.*, UCSF Chimera--a visualization system for exploratory research and analysis. *J Comput Chem* **25**, 1605-1612 (2004).
55. D. Liebschner *et al.*, Macromolecular structure determination using X-rays, neutrons and electrons: recent developments in Phenix. *Acta Crystallographica Section D: Structural Biology* **75**, 861-877 (2019).
56. P. Emsley, K. Cowtan, Coot: model-building tools for molecular graphics. *Acta Crystallogr D Biol Crystallogr* **60**, 2126-2132 (2004).
57. P. V. Afonine *et al.*, Real-space refinement in PHENIX for cryo-EM and crystallography. *Acta Crystallogr D Struct Biol* **74**, 531-544 (2018).
58. O. S. Smart, J. G. Neduvelil, X. Wang, B. Wallace, M. S. Sansom, HOLE: a program for the analysis of the pore dimensions of ion channel structural models. *Journal of molecular graphics* **14**, 354-360 (1996).
59. D. C. Bas, D. M. Rogers, J. H. Jensen, Very fast prediction and rationalization of pKa values for protein-ligand complexes. *Proteins* **73**, 765-783 (2008).
60. W. L. Jorgensen, J. Chandrasekhar, J. D. Madura, R. W. Impey, M. L. Klein, Comparison of simple potential functions for simulating liquid water. *J. Chem. Phys.* **79**, 926-935 (1983).
61. W. Humphrey, A. Dalke, K. Schulten, VMD: Visual molecular dynamics. *Journal of Molecular Graphics* **14**, 33-38 (1996).
62. J. Yoo, A. Aksimentiev, Improved Parametrization of Li+, Na+, K+, and Mg2+ Ions for All-Atom Molecular Dynamics Simulations of Nucleic Acid Systems. *J. Phys. Chem. Lett.* **3**, 45–50 (2012).
63. J. Huang, A. D. MacKerell, CHARMM36 all-atom additive protein force field: Validation based on comparison to NMR data. *Journal of Computational Chemistry* **34**, 2135-2145 (2013).
64. J. C. Phillips *et al.*, Scalable molecular dynamics with NAMD. *Journal of Computational Chemistry* **26**, 1781-1802 (2005).
65. V. Rassolov, M. Ratner, J. Pople, P. Redfern, L. Curtis, 6-31G* basis set for third-row atoms *J. Comput. Chem.* **22**, 976-984 (2001).

bioRxiv preprint doi: https://doi.org/10.1101/2024.02.16.580716; this version posted February 21, 2024. The copyright holder for this preprint (which was not certified by peer review) is the author/funder, who has granted bioRxiv a license to display the preprint in perpetuity. It is made available under a CC-BY-NC-ND 4.0 International license.

66. J. J. P. Stewart, Optimization of Parameters for Semiempirical Methods .2. Applications. *Journal of computational chemistry* **10**, 221-264 (1989).
67. M. Frisch *et al.*, *Gaussian 09 Revision A.1*. (Gaussian Inc, 2009).

Acknowledgments

Cryo grid preparation and screening were carried out at the Cryo-EM Unit at Virginia Commonwealth University (VCU) supported by the VCU School of Medicine and M.S.'s funds. Cryo-EM data collection was carried out at the Frederick National Laboratory for Cancer Research supported by contract HSSN261200800001E where we thank Drs. Thomas Edwards, Ulrich Baxa and Adam Wier for cryo-EM data collection, and at the Molecular Electron Microscopy Core Facility at the University of Virginia (UVA) (supported by NIH U24 GM116790). Supported by NIH R01 AR068431 and U24GM116790 (to M.S.) and Thailand Science research and Innovation Fund Chulalongkorn University HEA662300080 (to P.S.).

Author contributions

ARN, AHW, PCH and YH performed protein purification and cryo-grid preparation; KD assisted with data collection; ARN, JJL and AHW performed image processing; ARN performed model building and radioligand binding assays; PS and WR carried out molecular dynamics, quantum chemical calculations and validation; MS conceived, designed, and supervised all cryo-EM experiments; MS, PS and ARN interpreted the data and wrote the manuscript; AHW edited the manuscript; GDL provided valuable intellectual input.

Competing interests

Authors declare that they have no competing interests.

Data availability

Cryo-EM maps of RyR1-ACP/LMg^{2+} and RyR1-ACP/HMg^{2+} deposited in the Electron Microscopy Databank (EMDB) with accession codes 22615 and 26610, respectively. Atomic models generated from cryo-EM maps of RyR1-ACP/LMg^{2+} and RyR1-ACP/HMg^{2+} are deposited in the PDB database with accession codes 7K0S and 7UMZ respectively.

bioRxiv preprint doi: https://doi.org/10.1101/2024.02.16.580716; this version posted February 21, 2024. The copyright holder for this preprint (which was not certified by peer review) is the author/funder, who has granted bioRxiv a license to display the preprint in perpetuity. It is made available under a CC-BY-NC-ND 4.0 International license.

Figures

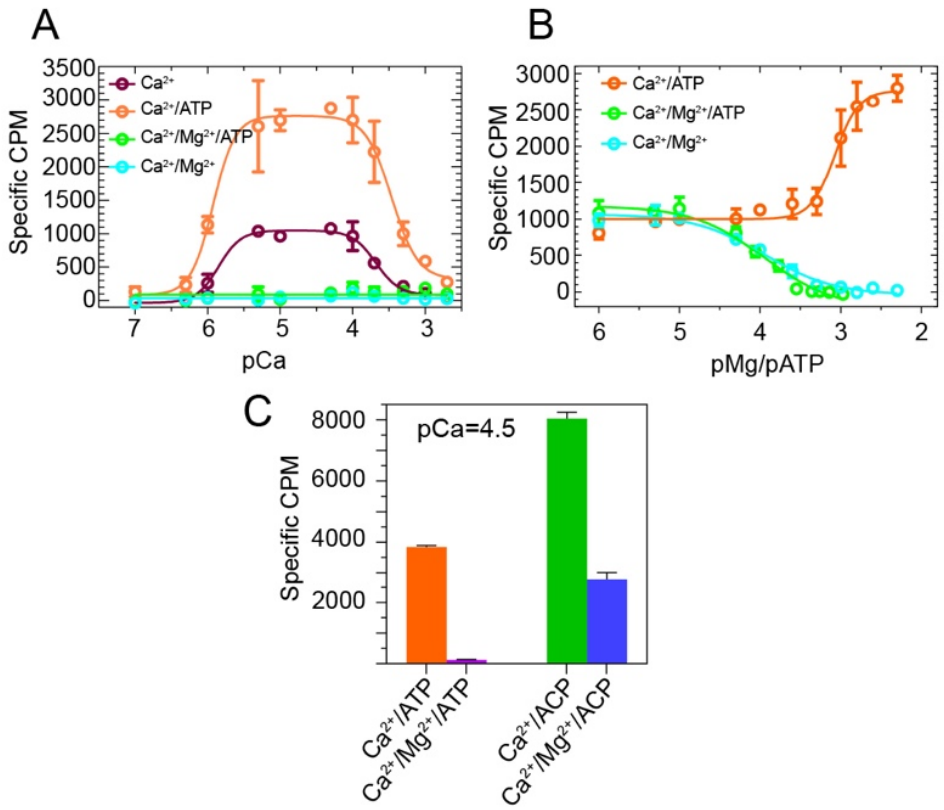


Figure 1. Inhibition of RyR1 by Mg^{2+}. **A,** Ryanodine binding to rabbit skeletal SR membrane vesicles demonstrates a biphasic response of RyR1 over a wide range of Ca^{2+} concentrations (100 nM - 2 mM). At all Ca^{2+} concentrations, ATP (2 mM) increased ryanodine binding, whereas Mg^{2+} alone (1 mM) or Mg^{2+}/ATP (5 mM each) abolished channel activity. **B**, Progressive inhibition of RyR1 by Mg^{2+} (from 1 µM to 5 mM) in the presence or absence of equivalent concentrations of ATP, and progressive activation of RyR1 by ATP (from 1 µM to 5 mM). Ca^{2+} concentration was 50 µM for all data points. **C,** At 50 µM Ca^{2+}, Mg^{2+}/ATP (5 mM each) abrogated RyR1 opening completely, while substitution of ATP by AMP-PCP resulted in further activation of the channel and incomplete inhibition by Mg^{2+}, respectively. Data represent mean ± SEM specific [^{3}H]-ryanodine binding from three independent experiments.

bioRxiv preprint doi: https://doi.org/10.1101/2024.02.16.580716; this version posted February 21, 2024. The copyright holder for this preprint (which was not certified by peer review) is the author/funder, who has granted bioRxiv a license to display the preprint in perpetuity. It is made available under a CC-BY-NC-ND 4.0 International license.

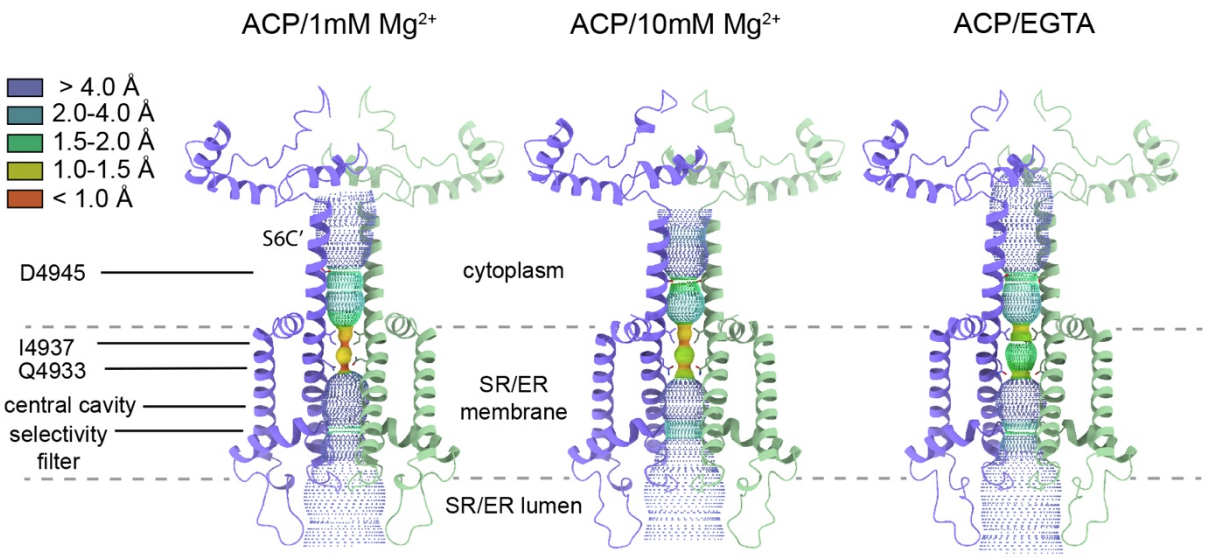


Figure 2. **Pore profiles of RyR1-ACP/Mg^{2+} and ACP/EGTA**. Protein-excluded dotted surfaces showing the ion permeation pathway and cytoplasmic extension of the S6 helical bundle (S6C') of RyR1 in the presence of Mg^{2+} (this work) and in the presence of EGTA (PDB ID: 7K0T). Landmarks include the hydrophobic (I4937) and polar gating residue (Q4933) at the ion gate, and the negatively charged ring at D4945 in S6C'. Residues 4821-5037 of two subunits in diagonal are displayed. The dashed lines indicate the approximate boundaries of the membrane.

bioRxiv preprint doi: https://doi.org/10.1101/2024.02.16.580716; this version posted February 21, 2024. The copyright holder for this preprint (which was not certified by peer review) is the author/funder, who has granted bioRxiv a license to display the preprint in perpetuity. It is made available under a CC-BY-NC-ND 4.0 International license.

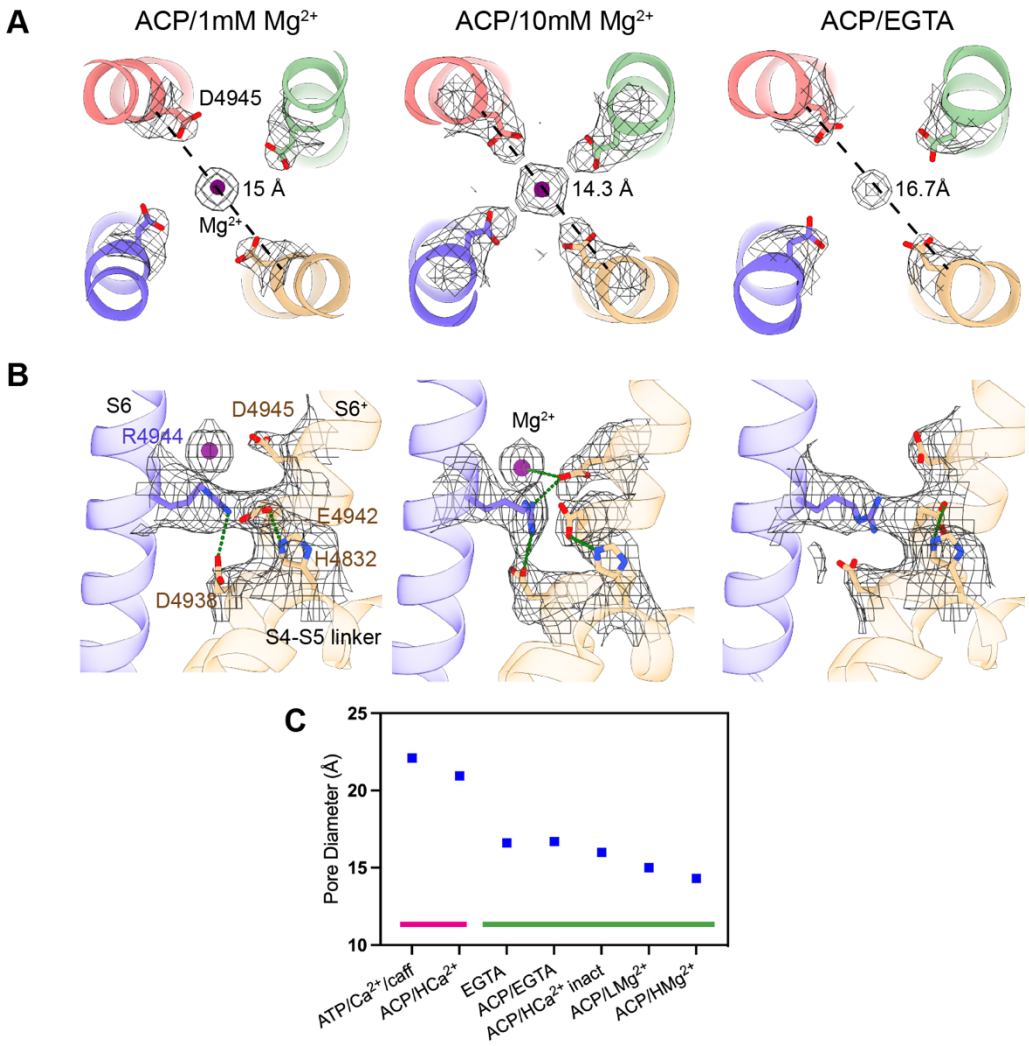


Figure 3. Concentration-dependent effect of Mg^{2+} on the pore of RyR1. A, Fourfold cytoplasmic views of the S6C' extension. The ring formed by D4945 shrinks by 1.7-2.4 Å in the presence of Mg^{2+} (purple). Pore diameter measured from the diagonal helices (Cα atom) is shown. Coulombic density around the putative Mg^{2+} site is displayed in mesh. Density attributed to Mg^{2+} in RyR1-ACP/10mM Mg^{2+} can be seen up to 11 σ. **B,** Mg^{2+} binding to the D4945 site forms a tripartite bridge between neighboring inner helices (S6) in the ACP/HMg^{2+} condition. The interaction network, D4945-R4944-D4938, and E4942-H4832, extends from the centrally coordinated Mg^{2+} ion to the S4-S5 linker (via S6). The structures obtained at low Mg^{2+} or without Mg^{2+} lack such an interaction network. **C,** Comparison of the pore diameter (measured between opposite C_α of D4945) of RyR1 under different conditions. Magenta line indicates open channels, green line indicates closed channels. The conditions and PDB IDs are as follows: ATP/30μM Ca^{2+}/caffeine open (5TAL), ACP/2 mM Ca^{2+} open (7TDH), metal-free (EGTA; 5TB0), ACP/EGTA (7K0T), ACP/2 mM Ca^{2+} inactivated (7TDG), ACP/1 mM Mg^{2+} (7K0S; this work), ACP/10 mM free Mg^{2+} closed (7UMZ; this work). The four conditions on the right correspond to channels prepared in identical conditions except for the divalent metal. The cytoplasmic portion of the S6 bundle is narrowest in the presence of Mg^{2+}.

bioRxiv preprint doi: https://doi.org/10.1101/2024.02.16.580716; this version posted February 21, 2024. The copyright holder for this preprint (which was not certified by peer review) is the author/funder, who has granted bioRxiv a license to display the preprint in perpetuity. It is made available under a CC-BY-NC-ND 4.0 International license.

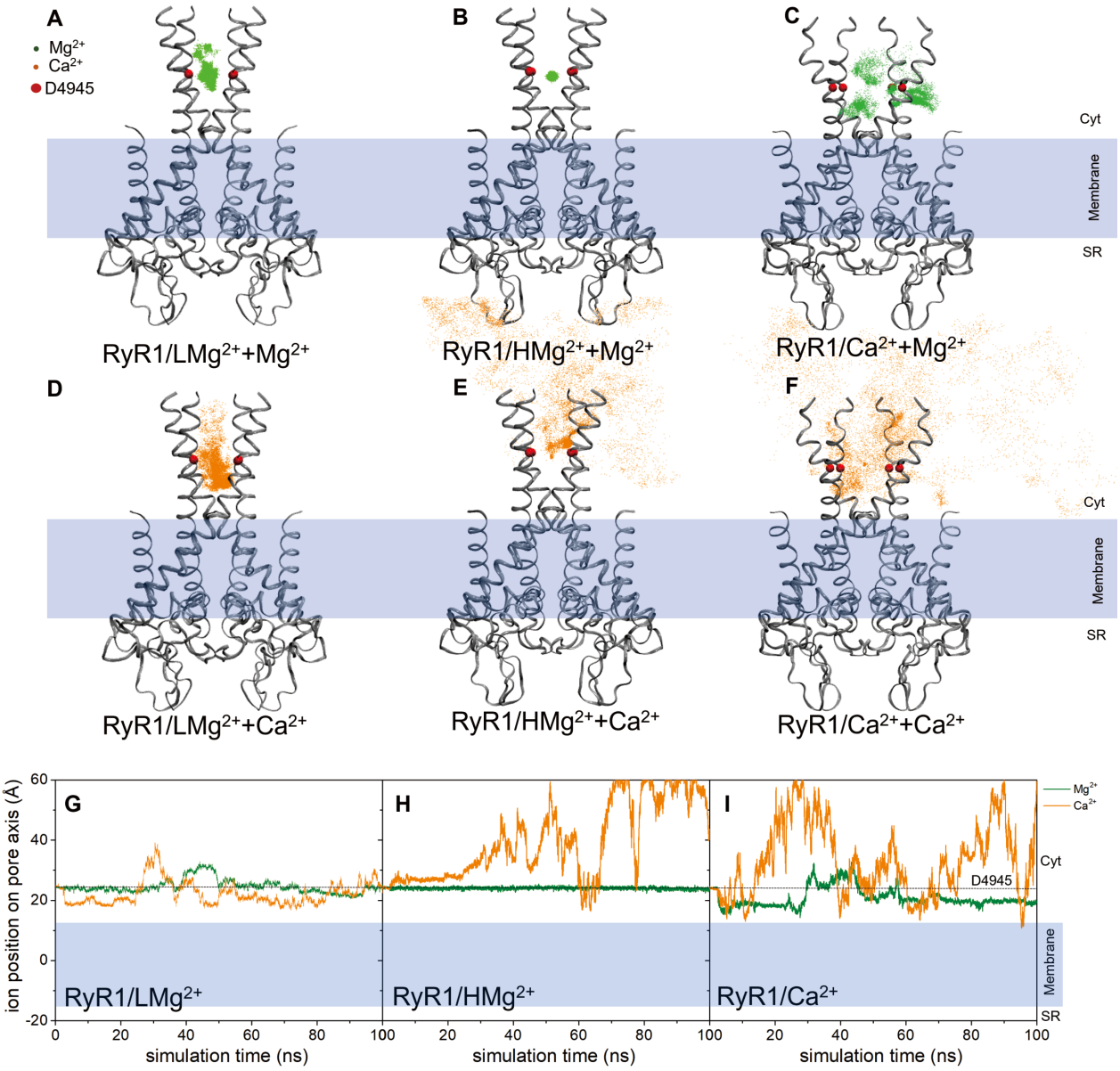


Figure 4. Molecular dynamics of the pore domain. A-F, Displacement of Mg^{2+} and Ca^{2+} ions is depicted with green and orange dots, respectively, at the D4945 site (red spheres) during 100ns MD simulations. Each dot represents a collection of MD snapshots taken at intervals of 0.02ns. The ribbon structures of the RyR1 pore domain in various conformations are illustrated in their initial configurations. **G-I**, Ion displacement in relation to the z-axis of the channel over the course of simulation time. Note that return to the original z position can occur via the outside of the pore domain.

bioRxiv preprint doi: https://doi.org/10.1101/2024.02.16.580716; this version posted February 21, 2024. The copyright holder for this preprint (which was not certified by peer review) is the author/funder, who has granted bioRxiv a license to display the preprint in perpetuity. It is made available under a CC-BY-NC-ND 4.0 International license.

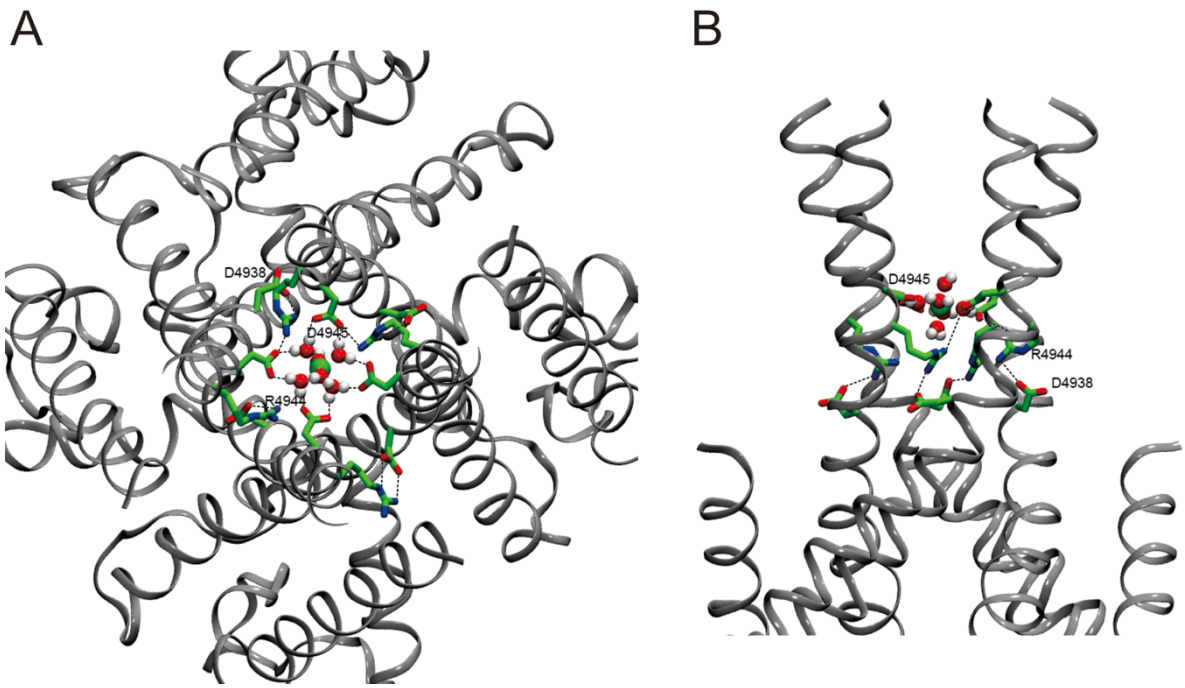


Figure 5. MD snapshot of RyR1/HMg^{2+} + Mg^{2+}. **A**, Cytoplasmic view illustrating the involvement of the D4945 carboxyl oxygens in hydrogen bond interactions with first-shell water molecules, leading to stabilization of Mg^{2+} (green sphere) at this site. **B**, Side view showcasing the hydrogen bond network involving D4945, R4944, D4938, and Mg^{2+}.

bioRxiv preprint doi: https://doi.org/10.1101/2024.02.16.580716; this version posted February 21, 2024. The copyright holder for this preprint (which was not certified by peer review) is the author/funder, who has granted bioRxiv a license to display the preprint in perpetuity. It is made available under a CC-BY-NC-ND 4.0 International license.

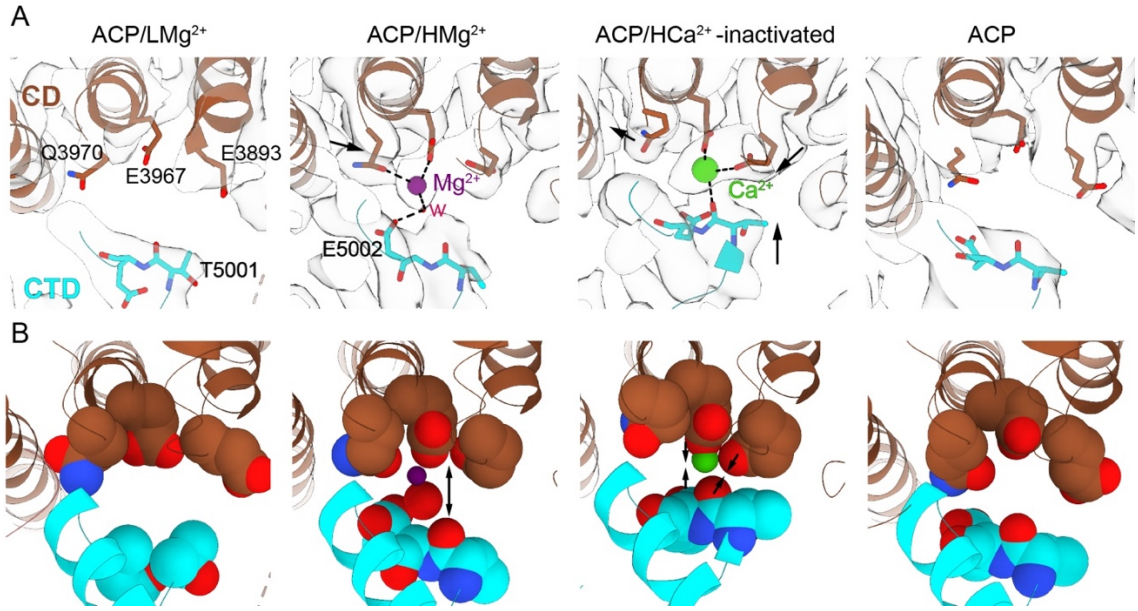


Figure 6. Binding of Mg^{2+} at the high-affinity Ca^{2+} activation site. A, Cryo-EM of the Ca^{2+} binding site at the CD/CTD interface reveals a shared binding site. At low Mg^{2+} concentration, the site is empty. At high Mg^{2+} concentration, the site is occupied by partially hydrated Mg^{2+}, which imposes a different configuration compared to the Ca^{2+} ion. In contrast to Ca^{2+} binding to E3893, E3967, and the carbonyl of T5001, Mg^{2+} binds to E3967, Q3970, and a water molecule connected to E5002 (distances < 3 Å), but it is separated from E3893 (4.7 Å). Coulombic densities surrounding the divalent binding site are depicted in the respective cryo-EM maps. The 3D reconstructions of RyR1 without Ca^{2+} (PDB ID: 7K0T) or Ca^{2+}-inactivated RyR1 (PDB ID: 7TDG) are shown for comparison; see Fig. S4 for RyR1 in the open state. Arrows indicate the conformational changes effected by Mg^{2+} or Ca^{2+}. Pore axis is on the left. **B,** Space-filling representation of the Ca^{2+} activation site. Mg^{2+} and its water of hydration cause slight expansion of the cavity, indicated by separation of T5001-E3967 by 1Å and lack of interaction with E3893 in RyR1-ACP/HMg^{2+}. In contrast, in the Ca^{2+}-inactivated structure, Ca^{2+} gravitates towards E3893, releasing Q3970, and the T5001-E3893 contact shrinks by ~2 Å closing the cavity on the E3893 side.

bioRxiv preprint doi: https://doi.org/10.1101/2024.02.16.580716; this version posted February 21, 2024. The copyright holder for this preprint (which was not certified by peer review) is the author/funder, who has granted bioRxiv a license to display the preprint in perpetuity. It is made available under a CC-BY-NC-ND 4.0 International license.

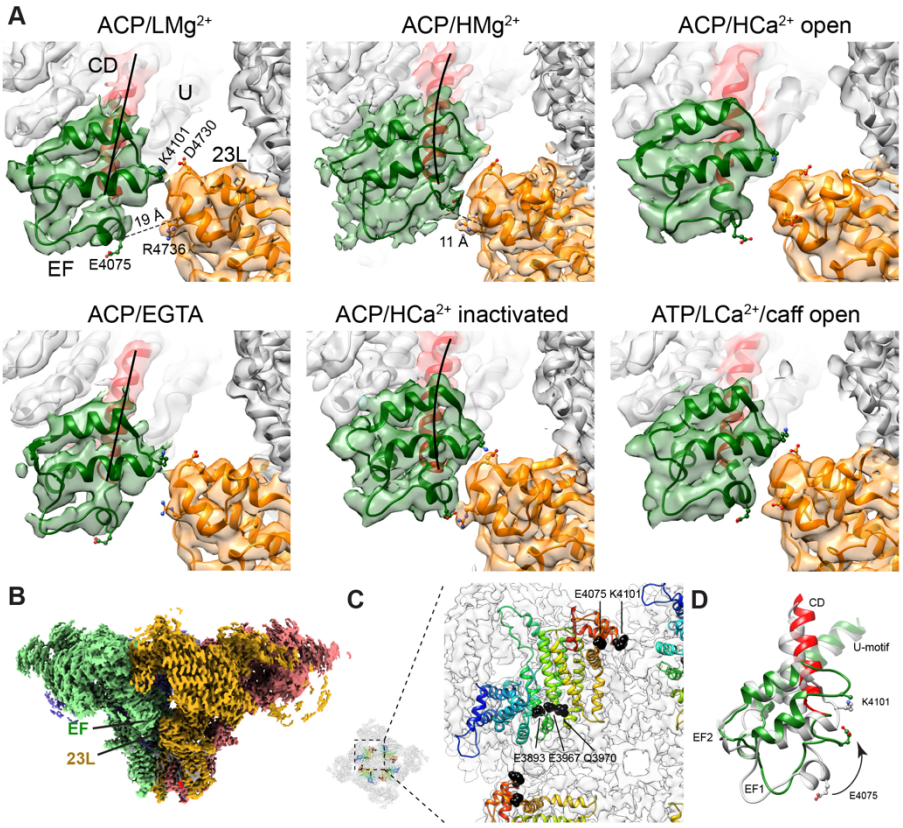


Figure 7. Mg^{2+}-induced conformational changes at the EF-hand domain in the context of closed, inactivated, and open channels. A, Transition from the ACP/LMg^{2+} to the ACP/HMg^{2+} condition results in a conformational change in the EF hand domain (green). A rotation of the domain concomitant with a tilt in the incoming alpha helix (residues 4053-4070 from the CD, in red, with helical axis indicated with a black line) approximates E4075 and R4736 from ~19 Å to ~11 Å (measured at the Cα). This orientation enables formation of two salt bridges with the S2-S3 cytoplasmic extension (23L; orange) of the neighboring subunit. Transition from ACP/EGTA to ACP/HCa^{2+}-inactivated conditions undergoes an analogous conformational change (each shown below for comparison). In open RyR1s, induced either by 2 mM Ca^{2+} or by 30 μM Ca^{2+} plus ATP and caffeine, the EF hand domain moves less than in the HCa^{2+} or HMg^{2+} conditions. **B,** Side view of RyR1 with one EF hand domain and S2-S3 cytoplasmic loop facing the viewer. Each subunit is displayed in a different color. The most proximal part of the cytoplasmic shell is removed for clarity. **C,** Relative position of the EF hands and CD seen from the TMD side. The polypeptide chain is color-coded from blue at the CD N' terminus to red at the EF hand C' terminus. The three CAS residues in the CD and the two salt-bridge forming EF hand residues are indicated. Proximity between the CAS and the EF hand domain suggests inter-dependence of movement (see also Movie S4), however the higher amplitude of the EF hand domain and detachment of the incoming alpha helix from the rest of the CD indicates the ability to move independently. **D,** Conformational change of the EF hand upon increasing the free Mg^{2+} concentration from 1 mM (gray) to 10 mM (red and green as in panel A). Coordination of Mg^{2+} by the negative charges of the EF loops likely underlies the conformational change.

bioRxiv preprint doi: https://doi.org/10.1101/2024.02.16.580716; this version posted February 21, 2024. The copyright holder for this preprint (which was not certified by peer review) is the author/funder, who has granted bioRxiv a license to display the preprint in perpetuity. It is made available under a CC-BY-NC-ND 4.0 International license.

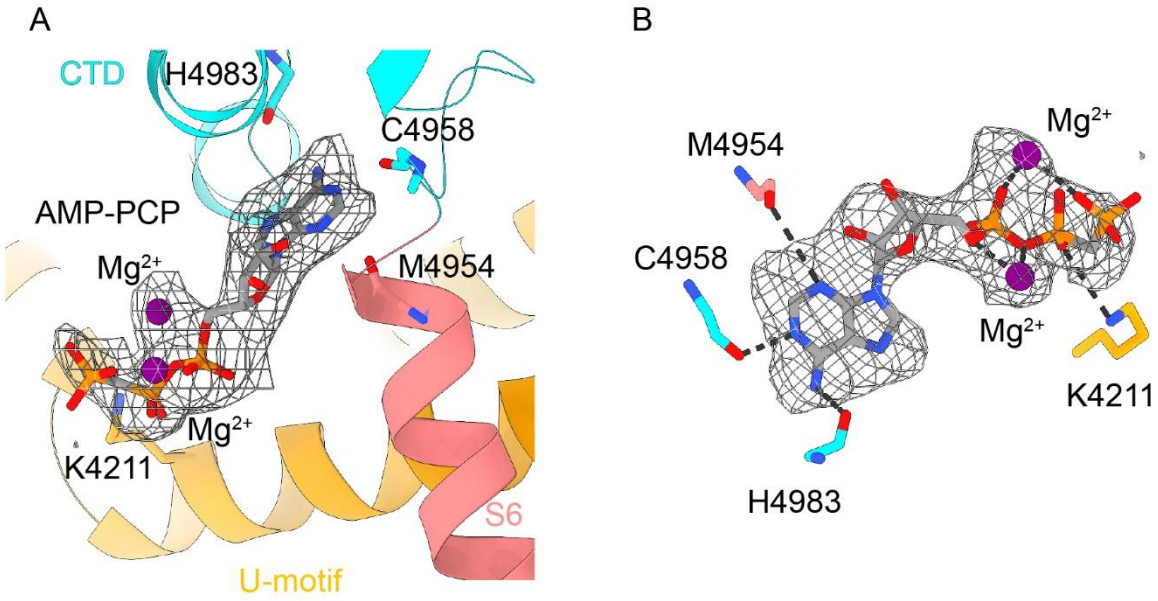


Figure 8. Mg^{2+} forms a stable complex with ACP at the U-motif-S6-CTD- interface. **A,** An ACP (AMP-PCP) molecule bound to the U-motif, S6C' and CTD domain interface contains two additionally coordinated Mg^{2+} ions clearly visible in the ACP/HMg^{2+} condition. **B,** Densities attributed to two Mg^{2+} ions and ACP in the ACP/HMg^{2+} cryo-EM focused map at 2.8 Å resolution. The Mg^{2+} on top adopts a bidentate geometry with the terminal oxygens of alpha and gamma phosphates, whereas the Mg^{2+} at the bottom coordinates with the oxygens from the ACP backbone.

bioRxiv preprint doi: https://doi.org/10.1101/2024.02.16.580716; this version posted February 21, 2024. The copyright holder for this preprint (which was not certified by peer review) is the author/funder, who has granted bioRxiv a license to display the preprint in perpetuity. It is made available under a CC-BY-NC-ND 4.0 International license.

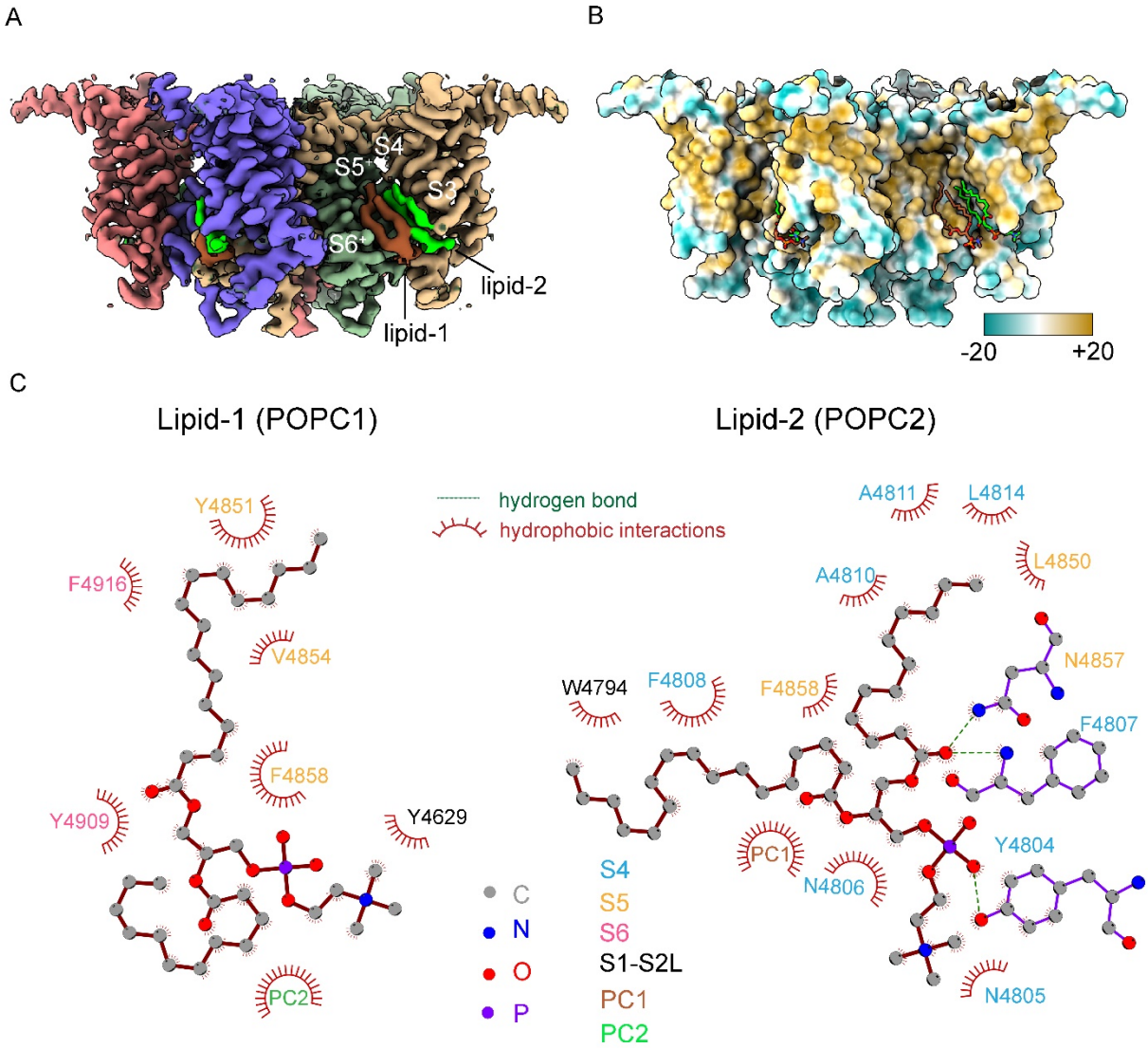


Figure 9. A lipophilic crevice of RyR1 binds two lipids in the presence of ACP/HMg^{2+}. **A,** Density for the transmembrane domain and bound lipids in the 2.8 Å resolution cryo-EM map focused on the central and transmembrane domains. The two partial lipids are part of two PC16:0/18:1 molecules that bind to a domain-swapped crevice formed by S3/S4 and S5/S6 helices of neighboring subunits. **B,** Molecular lipophilicity potential map of the transmembrane domain showing a hydrophobic pocket (yellow) where two lipids are bound. Hydrophilic and hydrophobic amino acids are colored cyan and yellow, respectively. **C,** The two lipids are stabilized by contacts with S5/S6, S1-S2 loop (POPC1; left) and S4/S5 (POPC2; right), mediated by their hydrophilic head and hydrophobic tail. Hydrogen bond and hydrophobic contact distances shown are below 3.4 Å and 3.9 Å respectively.

bioRxiv preprint doi: https://doi.org/10.1101/2024.02.16.580716; this version posted February 21, 2024. The copyright holder for this preprint (which was not certified by peer review) is the author/funder, who has granted bioRxiv a license to display the preprint in perpetuity. It is made available under a CC-BY-NC-ND 4.0 International license.

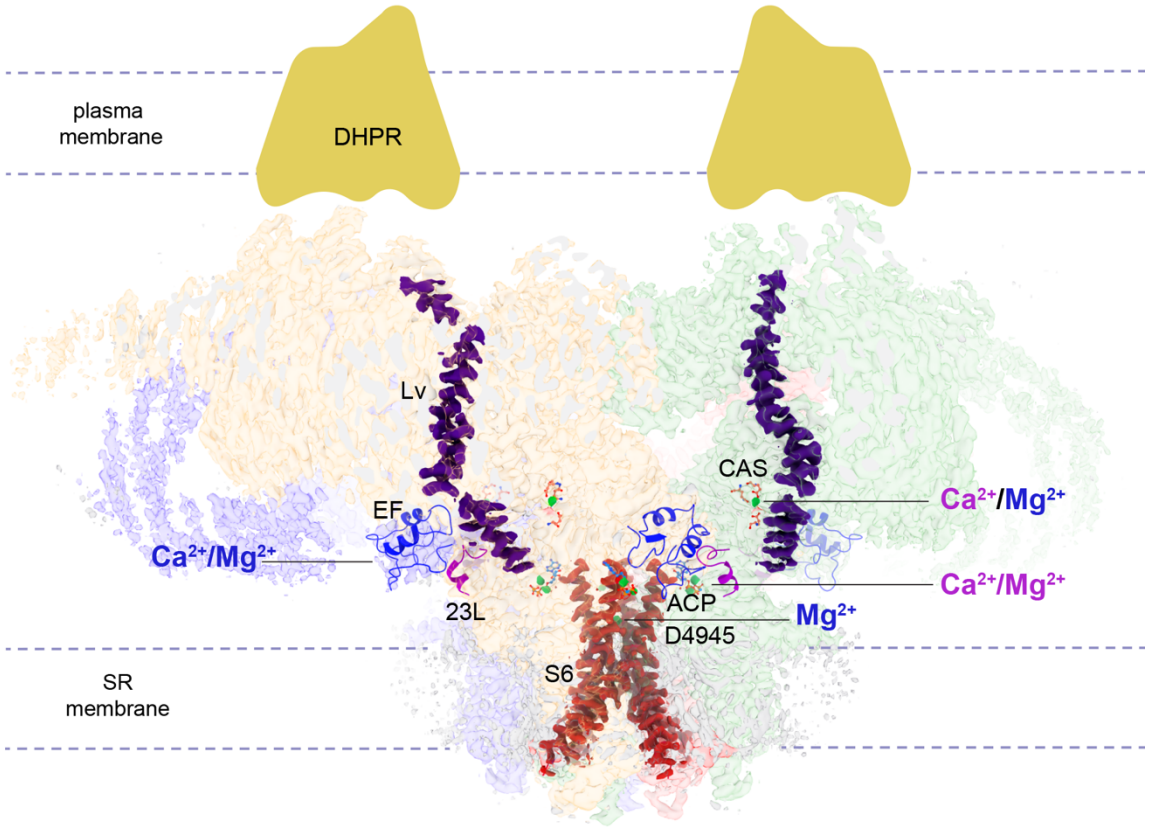


Figure 10. Multiple Mg^{2+} and Ca^{2+} binding sites within RyR1. At each site the divalent cations act as activators (magenta font), as inhibitors (blue font), or serve other roles (black font). The high affinity Ca^{2+} activation site (CAS) exhibits a lower affinity for Mg^{2+} with an opposing effect. The EF hands are proposed to function as a low affinity, inhibitory Ca^{2+}/Mg^{2+} module that binds to the S2-S3 cytoplasmic loop (23L; partially shown for clarity) of the neighboring subunit. Binding of either Ca^{2+} (*26*) or Mg^{2+} to the ATP site is likely to enhance structural continuity between its neighboring domains (U motif, S6, and CTD). Binding of Mg^{2+} to the D4945 site at the fourfold axis tightens the S6 helical bundle, while no binding of Ca^{2+} is observed at this site. We hypothesize that four long levers (Lv; only two shown for clarity) provide a long-range allosteric pathway conveying the excitatory input from the DHPR to RyR1's stem region. Abatement of the levers induced by conformational coupling, or binding of Ca^{2+} to the CAS, is expected to trigger the separation of S6, resulting in the removal of Mg^{2+} coordination at the D4945 site. Resolved cryo-EM globular densities attributed to Mg^{2+} are shown in green. The side view of the RyR1 cryo-EM density has the front and back partially omitted for clarity; densities for S6 and the levers are highlighted.